# Thermal Decomposition of $NH_2OH$ and Subsequent Reactions: Ab Initio Transition State Theory and Reflected Shock Tube Experiments

**S. J. Klippenstein,* L. B. Harding,* B. Ruscic, R. Sivaramakrishnan, N. K. Srinivasan, M.-C. Su,† and J. V. Michael***

*Chemical Sciences and Engineering Division, Argonne National Laboratory, Argonne, Illinois 60439, USA*

*Received: June 10, 2009; Revised Manuscript Received: July 21, 2009*

Primary and secondary reactions involved in the thermal decomposition of $NH_2OH$ are studied with a combination of shock tube experiments and transition state theory based theoretical kinetics. This coupled theory and experiment study demonstrates the utility of $NH_2OH$ as a high temperature source of OH radicals. The reflected shock technique is employed in the determination of OH radical time profiles via multipass electronic absorption spectrometry. O-atoms are searched for with atomic resonance absorption spectrometry. The experiments provide a direct measurement of the rate coefficient, $k_1$, for the thermal decomposition of $NH_2OH$. Secondary rate measurements are obtained for the $NH_2 + OH$ (5a) and $NH_2OH + OH$ (6a) abstraction reactions. The experimental data are obtained for temperatures in the range from 1355 to 1889 K and are well represented by the respective rate expressions: $\log[k/(\mathrm{cm^3\ molecule^{-1}\ s^{-1}})] = (-10.12 \pm 0.20) + (-6793 \pm 317\ \mathrm{K}/T)$ ($k_1$); $\log[k/(\mathrm{cm^3\ molecule^{-1}\ s^{-1}})] = (-10.00 \pm 0.06) + (-879 \pm 101\ \mathrm{K}/T)$ ($k_{5a}$); $\log[k/(\mathrm{cm^3\ molecule^{-1}\ s^{-1}})] = (-9.75 \pm 0.08) + (-1248 \pm 123\ \mathrm{K}/T)$ ($k_{6a}$). Theoretical predictions are made for these rate coefficients as well for the reactions of $NH_2OH + NH_2$, $NH_2OH + NH$, $NH + OH$, $NH_2 + NH_2$, $NH_2 + NH$, and $NH + NH$, each of which could be of secondary importance in $NH_2OH$ thermal decomposition. The theoretical analyses employ a combination of ab initio transition state theory and master equation simulations. Comparisons between theory and experiment are made where possible. Modest adjustments of predicted barrier heights (i.e., by 2 kcal/mol or less) generally yield good agreement between theory and experiment. The rate coefficients obtained here should be of utility in modeling $NO_x$ in various combustion environments.

## Introduction

Bimolecular reaction rate studies at high-$T$ ($T > 1000$ K) of OH with saturated hydrocarbons, RH, are important in combustion since OH is the most reactive chain center in branching chain oxidations.[1] Unfortunately, most of the direct experimental measurements have been limited to $T < 1000$ K due to the unavailability of a clean high-$T$ thermal source for generating OH-radicals. The studies by Bott and Cohen,[2] who used a reflected shock tube technique at $T = \sim 1200$ K, and studies of OH with hydrocarbons from this laboratory,[3] are the only exceptions. These studies used tBH (*tert*-butyl hydroperoxide) as an OH source. This molecule rapidly dissociates and is relatively easy to handle, but it cannot be used at $T > \sim 1300$ K in reflected shock tube work because the compound is unstable and starts to significantly decompose to $(CH_3)_2CO$, OH, and $CH_3$ in the incident shock regime.[3] The reaction $H + NO_2 \rightarrow OH + NO$ using $C_2H_5I/NO_2$ mixtures has been previously used in this laboratory[4] and is indeed an effective method for generating a fast OH concentration pulse compared to the time duration for kinetics experiments. However, this method utilizes excess $NO_2$, complicating the kinetics as well as contributing to the profile signal at 308 nm due to $NO_2$ absorption. Furthermore, it is limited to $T < 2000$ K due to interferences from $C_2H_4$, which dissociates at high-$T$ yielding additional H-atoms that can also react directly with excess $NO_2$ giving additional OH. $HNO_3$ and $CH_3OH$ have also been used at high-$T$ (>1800 K) in our laboratory,[3,5] but the former is difficult to prepare and handle even in a greaseless all glass vacuum line.

In this work, we have studied, for the first time, the thermal decomposition of hydroxylamine, $NH_2OH$. The motivation and goal of the study is to demonstrate the possibility of using this molecule as another OH-radical source for bimolecular reaction studies at somewhat lower-$T$ than is possible with $CH_3OH$, thereby bridging the temperature gap between $CH_3OH$ and tBH sources. The utility of this new OH source was demonstrated in our recent study of the reactions of OH with acetylene and ethylene.[5] The present analysis of the $NH_2OH$ decomposition employs a combination of theory and experiment to explore the products and rate coefficient. High level ab initio calculations suggest two possible product channels, $NH_2 + OH$ and $NH_3 + O$. Experimental observations of the OH and O time profiles demonstrate that only the $NH_2 + OH$ channel is significant.

The experimentally observed OH profiles arising from the $NH_2OH$ decomposition are found to have secondary sensitivity to two additional reactions, namely, $NH_2OH + OH \rightarrow$ products and $NH_2 + OH \rightarrow NH + H_2O$. For these reactions, rate constants were also determined both experimentally and theoretically. In addition, there is little known about the rate coefficients for the subsequent reactions of $NH_2$ and NH. A

* Corresponding authors. J. V. M.: address, Rm. D-193, Bldg. 200, Argonne National Laboratory, Argonne, IL 60439; phone: (630) 252-3171; fax: (630) 252-9570; e-mail: jmichael@anl.gov; S. J. Klippenstein: address, Bldg. 200, Argonne National Laboratory, Argonne, IL 60439; phone: (630) 252-3596; fax: (630) 252-9292; e-mail: sjk@anl.gov; L. B. Harding: address, Bldg. 200, Argonne National Laboratory, Argonne, IL 60439; phone: (630) 252-3591; fax: (630) 252-9292; e-mail: harding@anl.gov.

† Special Term Appointment, Argonne. Permanent address: Department of Chemistry, Sonoma State University, 1801 E. Cotati Ave., Rohnert Park, CA 94928.

10.1021/jp905454k CCC: $40.75 
Published on Web 09/01/2009

**TABLE 1: Thermochemistry at 0 K from Active Thermochemical Tables[a] for Reactions $NH_2OH \rightarrow$ Products, $NH_2OH + X$ (X = OH, $NH_2$, and NH) $\rightarrow$ Products, OH + NH $\rightarrow$ Products, NH + NH $\rightarrow$ Products, NH + $NH_2 \rightarrow$ Products, and $NH_2 + NH_2 \rightarrow$ Products**

| reaction | ATcT energy (kcal/mol) |
|---|---|
| $NH_2OH \rightarrow$ Products | |
| $NH_2 + OH$ | 0[b] |
| $NH_2OH$ | $-62.01 \pm 0.13$[b] |
| $^3NH + H_2O$ | $-25.43 \pm 0.05$[b] |
| $NH_3 + {}^3O$ | $-4.30 \pm 0.04$[b] |
| $^1NH + H_2O$ | $10.57 \pm 0.06$[b] |
| $H_2NO + H$ | $14.59 \pm 0.24$[b] |
| $HNOH + H$ | $21.87 \pm 0.30$[b] |
| $NH_3 + {}^1O$ | $41.07 \pm 0.04$[b] |
| $NH_2OH + OH \rightarrow$ Products | |
| $NH_2OH + OH$ | 0[c] |
| $H_2NO + H_2O$ | $-41.05 \pm 0.24$[c] |
| $HNOH + H_2O$ | $-33.76 \pm 0.31$[c] |
| $NH_2OH + NH_2 \rightarrow$ products | |
| $NH_2OH + NH_2$ | 0[d] |
| $H_2NO + NH_3$ | $-29.43 \pm 0.24$[d] |
| $HNOH + NH_3$ | $-22.15 \pm 0.31$[d] |
| $NH_2OH + NH \rightarrow$ Products | |
| $NH_2OH + NH$ | 0[e] |
| $H_2NO + NH_2$ | $-15.62 \pm 0.24$[e] |
| $HNOH + NH_2$ | $-8.33 \pm 0.31$[e] |
| $OH + NH \rightarrow$ Products | |
| $OH + NH$ | 0[f] |
| $H_2NO$ | $-77.62 \pm 0.24$[f] |
| $HNOH$ | $-70.34 \pm 0.31$[f] |
| $H_2 + NO$ | $-73.00 \pm 0.05$[f] |
| $N + H_2O$ | $-39.29 \pm 0.05$[f] |
| $HNO + H$ | $-16.75 \pm 0.06$[f] |
| $NH_2 + O$ | $9.51 \pm 0.06$[f] |
| $NH + NH \rightarrow$ Products | |
| $NH + NH$ | 0[g] |
| $N_2 + H_2$ | $-171.50 \pm 0.09$[g] |
| $HNNH$ | $-121.90 \pm 0.17$[g] |
| $H_2NN$ | $-97.84 \pm 0.23$[g] |
| $N_2 + H + H$ | $-68.23 \pm 0.09$[g] |
| $NNH + H$ | $-59.66 \pm 0.21$[g] |
| $N + NH_2$ | $-13.86 \pm 0.09$[g] |
| $NH + NH_2 \rightarrow$ Products | |
| $NH + NH_2$ | 0[h] |
| $N_2 + H_2 + H$ | $-79.29 \pm 0.07$[h] |
| $HNNH_2$ | $-74.68 \pm 0.30$[h] |
| $HNNH + H$ | $-29.69 \pm 0.17$[h] |
| $N + NH_3$ | $-27.67 \pm 0.07$[h] |
| $H_2NN + H$ | $-5.63 \pm 0.23$[h] |
| $NH_2 + NH_2 \rightarrow$ Products | |
| $NH_2 + NH_2$ | 0[i] |
| $N_2 + H_2 + H_2$ | $-90.34 \pm 0.08$[i] |
| $H_2NNH_2$ | $-64.14 \pm 0.09$[i] |
| $HNNH + H_2$ | $-40.75 \pm 0.18$[i] |
| $H_2NN + H_2$ | $-16.69 \pm 0.23$[i] |
| $NH_3 + NH$ | $-13.81 \pm 0.08$[i] |
| $HNNH_2 + H$ | $17.54 \pm 0.30$[i] |

[a] References 50 and 51. [b] Energies relative to the $NH_2 + OH$ asymptote. [c] Energies relative to the $NH_2OH + OH$ asymptote. [d] Energies relative to the $NH_2OH + NH_2$ asymptote. [e] Energies relative to the $NH_2OH + NH$ asymptote. [f] Energies relative to the OH + NH asymptote. [g] Energies relative to the NH + NH asymptote. [h] Energies relative to the NH + $NH_2$ asymptote. [i] Energies relative to the $NH_2 + NH_2$ asymptote.

number of these reactions, specifically, $NH_2OH + NH_2 \rightarrow$ products, $NH_2OH + NH \rightarrow$ products, NH + OH, $NH_2 + NH_2$, NH + $NH_2$, and NH + NH might have a significant impact on the OH profiles. Thus, for these reactions a priori theoretical predictions of their rate coefficients were obtained and incorporated in the modeling of the OH time profiles. Finally, during the course of the theoretical analysis we have also obtained rate coefficient predictions for the $NH_2 + OH \rightarrow NH_3 + O$ reaction. These various reactions in the $NH_2OH$ decomposition system are also important in energetic materials and in the thermal de-$NO_x$ mechanism,[6−8] and the present rate estimates should prove useful for modeling such systems.

## Theory

**$NH_2OH$ Decomposition Pathways.** The thermal decomposition of $NH_2OH$ is complicated by the presence of both spin-allowed and spin-forbidden pathways. A fairly detailed theoretical analysis of these pathways was provided in a recent theoretical study of the NH + $H_2O$ reaction by Mackie and Bacskay.[9] For the spin-allowed dissociation, the lowest energy pathway involves simple bond fission to form $NH_2$ + OH:

$$NH_2OH \rightarrow {}^1[H_2N\cdots HO] \rightarrow NH_2 + OH \qquad (1)$$

Other spin-allowed channels are strongly disfavored kinetically due to either significantly greater product endothermicities ($H_2NO$ + H, $H_2O + {}^1NH$, HNOH + H, and $NH_3 + {}^1O$, at 15, 11, 22, and 41 kcal/mol relative to $NH_2$ + OH; see Table 1) or high and tight barriers along the decomposition path (HNO + $H_2$).

But there are two possible spin-forbidden pathways that are exothermic relative to $NH_2$ + OH, namely $^3NH + H_2O$ and $NH_3 + {}^3O$ at −25 and −4 kcal/mol, respectively. Hence, a theoretical study of the $NH_2OH$ potential surface has been undertaken with the goal of identifying whether either of these spin-forbidden pathways might be important. To make either of these sets of spin forbidden products, one must access an intersection between the singlet and triplet surfaces (most likely corresponding to large N−O distances), and one must transfer a hydrogen from one heavy atom to the other. These two events can occur in either order.

If we first stretch the NO bond to form a hydrogen-bonded $H_2N\cdots HO$ complex, this complex can then undergo intersystem crossing (ISC) followed by an intramolecular hydrogen abstraction forming either set of spin forbidden products as shown in mechanisms 2a and 2b.

$$NH_2OH \rightarrow {}^1[H_2N\cdots HO] \xrightarrow{ISC} {}^3[H_2N\cdots HO] \rightarrow NH_3 + {}^3O \qquad (2a)$$

$$\rightarrow {}^3NH + H_2O \qquad (2b)$$

Alternatively one can consider a (1,2) hydrogen migration forming either $H_2O\cdots NH$ or $H_3NO$ followed by a lengthening of the NO bond until a crossing with the triplet surface is reached, as shown in mechanisms 3 and 4.

$$NH_2OH \rightarrow {}^1[H_2O\cdots NH] \xrightarrow{ISC} {}^3NH + H_2O \qquad (3)$$

$$NH_2OH \rightarrow {}^1H_3NO \xrightarrow{ISC} NH_3 + {}^3O \qquad (4)$$

The energetics for these processes are illustrated schematically in Figures 1 and 2 and the corresponding stationary point

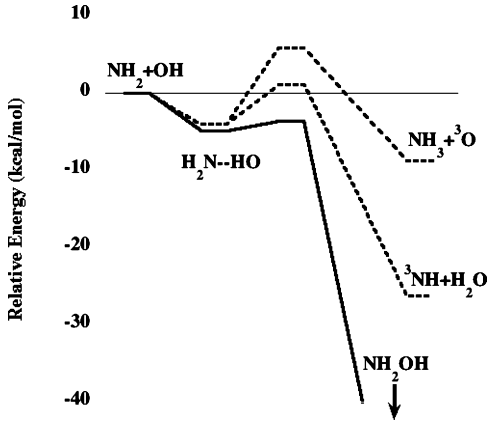


**Figure 1.** Schematic of calculated energies for mechanisms 2a and 2b. The solid lines correspond to the singlet state, the dashed to the triplet state.

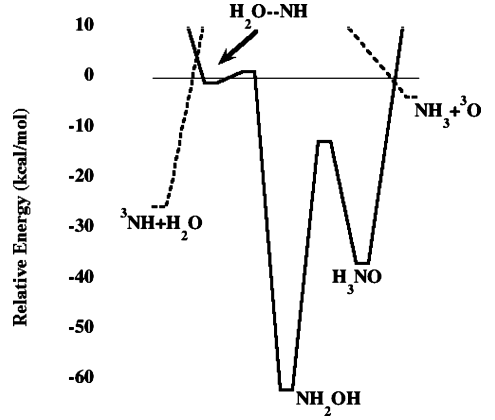


**Figure 2.** Schematic of calculated energies for mechanisms 3 and 4.

properties are provided in Table 2. With the exception of the $^1[H_2N\cdots HO]$ complex and the transition state for its formation, the energies of the stationary points in these two figures come from coupled cluster calculations with perturbative corrections for the effect of triple excitations [CCSD(T)].[10] Such CCSD(T) calculations are not appropriate for the $^1[H_2N\cdots HO]$ complex due to a high degree of multireference character. Thus, the energy of the $^1[H_2N\cdots HO]$ complex and related transition state were instead calculated, relative to the $NH_2$ + OH asymptote, using the internally contracted multireference, singles and doubles, configuration interaction (CAS+1+2)[11,12] method including the Davidson correction for higher level excitations (+QC).[13,14] In each case, the geometry optimizations and frequency analyses employed Dunning's augmented correlation consistent polarized valence double-$\zeta$ (aug-cc-pvdz) basis set.[15,16] The larger augmented triple and quadruple-$\zeta$ basis sets (aug-cc-pvqz) were then employed in determining more accurate energy estimates via extrapolation to the basis set limit.[17] The reference wave function used in the CAS+1+2+QC calculations was a three orbital, four electron CAS in which the three orbitals consist of the two OH p$\pi$ lone pairs and the radical orbital of the $NH_2$. Two state averaging was used in the CASSCF, orbital optimization step. The CCSD(T) and CAS+1+2+QC and other electronic structure calculations discussed below were all done with the MOLPRO program package.[18−22]

From Figure 1 we see that although singlet−triplet crossings for the hydrogen bonded complex are found at energies below that of the $NH_2$ + OH asymptote, the subsequent internal hydrogen abstractions are predicted to have barriers above the $NH_2$ + OH asymptote. Furthermore, the abstraction transition states should have lower entropy than for the bond fission transition state. Thus, (2a) and (2b) are not viable candidates for a second decomposition path. From Figure 2 we see that the initial hydrogen migration for mechanism 3 is predicted to have a barrier above the $NH_2$ + OH asymptote and would also have lower entropy. Thus, mechanism 3 is also ruled out as a viable candidate for a second decomposition path. However, for mechanism 4 the hydrogen migration barrier is predicted to be well below the $NH_2$ + OH asymptote, indicating that (4) may be important.

As a first step to locating the minimum singlet−triplet crossing for (4), we evaluated minimum energy paths for $H_3NO \rightarrow NH_3 + O$ on both the singlet and triplet surfaces. The results of these calculations, shown in Figure 3, demonstrate the existence of singlet−triplet crossings below the $NH_2$ + OH aymptote. A CCSD(T)/aug-cc-pvtz search for the minimum singlet−triplet crossing point in this region, using the Lagrangian method of Koga and Morokuma,[23] yields an energy of −2.3 kcal/mol, relative to $NH_2$ + OH. We conclude then that mechanism 4 is the only viable candidate for a second decomposition channel, and it is clear that if (4) contributes with rates similar to those for (1), then O-atoms should be produced at similar rates as OH-radicals. Hence, both [OH] and [O] have to be experimentally measured under similar conditions to assess this possibility.

**Kinetic Methodology.** The present theoretical predictions for the various rate coefficients employ a variety of electronic structure and rate theory methods. The rovibrational properties of the stationary points on the potential were generally determined with the CCSD(T) method employing either the aug-cc-pvdz or aug-cc-pvtz basis set. For cases with large multireference character, as indicated by a large T1 diagnostic,[24] for example, the stationary points were studied with multireference second-order perturbation theory (CASPT2)[25,26] and/or CAS+1+2+QC. In each instance, complete basis set estimates were obtained via extrapolation of aug-cc-pvtz and aug-cc-pvqz results. Spin orbit corrections for O and OH are included.

We have also implemented QCISD(T)[27] evaluations for a number of these multireference cases, particularly those involving abstraction reactions. When there is little multireference character, the CCSD(T) and QCISD(T) results are generally within about 0.1 kcal/mol. In contrast, for the abstraction reactions considered here, where the multireference character is generally quite significant, the QCISD(T) electronic barrier heights are all lower than the CCSD(T) barrier heights, with a typical difference being 0.8 kcal/mol. However, the zero-point corrections tend to be larger for the QCISD(T) method and so the net effect on the rate coefficient predictions is minimal. Thus, we present only the CCSD(T) results. In these CCSD(T) and QCISD(T) evaluations we generally employ the ROHF orbitals within the spin unrestricted coupled cluster formalism. If, instead, the spin restricted coupled cluster formalism is employed the barrier heights are significantly larger (∼1 kcal/mol) for these multireference abstraction cases.

For most transition states, rate coefficients were obtained from transition state theory employing rigid-rotor harmonic-oscillator energy assumptions for most degrees of freedom. Tunneling corrections based on asymmetric Eckart potentials and hindered rotor corrections for the torsional modes were included.

For the barrierless radical−radical reactions, the transition state partition functions were instead determined from variable reaction coordinate transition state theory.[28−30] The potential

**TABLE 2: Stationary Point Properties for the $NH_2OH$ System[a]**

| species | energy[b] (kcal/mol) | frequencies ($cm^{-1}$) | rotational constants ($cm^{-1}$) |
|---|---|---|---|
| $OH + NH_2$ | 0 | 3684 | 18.53, 18.53 |
| | | 3419, 3320, 1527 | 8.69, 12.80, 22.56 |
| $^3NH + H_2O$ | −25.4 | 3212 | 16.21, 16.21 |
| | | 3905, 3788, 1638 | 9.350, 14.43, 26.56 |
| $NH_3 + {}^3O$ | −3.7 | 3573, 3573, 3435, 1651 | 9.700, 9.700, 6.263 |
| | | 1651, 1071 | |
| $NH_2OH$ | −61.7 | 3803, 3503, 3413, 1637 | 0.828, 0.829, 6.270 |
| | | 1397, 1316, 1153, 888, 402 | |
| $H_3NO$ | −36.7 | 3341, 3341, 3268, 1642 | 0.876, 0.876, 6.059 |
| | | 1642, 1489, 1126, 1126, 935 | |
| $H_2O\cdots NH$ | −0.9 | 3841, 3740, 3353, 1623 | 0.644, 0.652, 6.103 |
| | | 1272, 734, 724, 495, 329 | |
| $H_2N\cdots HO$[c] | −4.1 | 3480, 3436, 3335, 1507 | 0.220, 0.224, 12.60 |
| | | 396, 389, 224, 222, 172 | |
| $NH_2 + OH \rightarrow {}^3NH + H_2O$[d] | 1.7 | 3703, 3350, 2220, 1361 | 0.322, 0.335, 8.243 |
| | (2.1) | 700, 608, 332, *468i*[d] | |
| $NH_2 + OH \rightarrow NH_3 + {}^3O$ (A″) | 6.1 | 3493, 3397, 1567, 1293 | 0.368, 0.372, 7.874 |
| | (7.6) | 1032, 770, 458, 420, *1937i* | |
| $NH_2 + OH \rightarrow NH_3 + {}^3O$ (A′) | 7.1 | | |
| $NH_2OH \rightarrow H_3NO$ | −12.5 | 3619, 3495, 2742, 1568 | 0.759, 0.767, 6.235 |
| | | 1223, 1024, 993, 703, *1635i* | |
| $NH_2OH \rightarrow H_2O\cdots NH$ | 1.4 | 3779, 3365, 2878, 1520 | 0.609, 0.627, 6.434 |
| | | 1181, 810, 549, 501, *948i* | |
| $NH_2OH \rightarrow H_2N\cdots HO$[c] | −3.5 | 3622, 3466, 3372, 1548 | 0.250, 0.252, 8.835 |
| | | 494, 447, 276, 136, *206i* | |
| $^1H_3NO \rightarrow NH_3 + {}^3O$ | −2.3[e] | | |

[a] Vibrational frequencies and rotational constants are CCSD(T)/CBS//CCSD(T)/aug-cc-pvdz values. For energies the primary values are CCSD(T)/CBS//CCSD(T)/aug-cc-pvdz results, while numbers in parentheses are CAS+1+2+QC(8,8)/CBS//CASPT2(8,8)/aug-cc-pvtz values. [b] Zero point corrected energy relative to $NH_2 + OH$. [c] These calculations are with the CAS+1+2+QC(4e,3o) method rather than CCSD(T). [d] There is also one low frequency mode that is treated as a hindered rotor. [e] CCSD(T)/aug-cc-pvtz calculation with no zero-point correction.

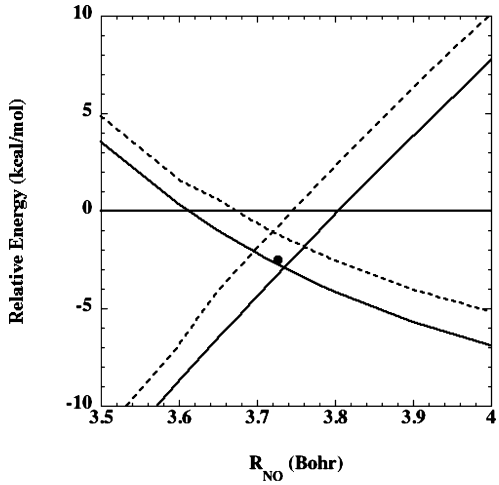


**Figure 3.** CCSD(T)/aug-cc-pvtz minimum energy paths (MEPs) for $H_3NO \rightarrow NH_3 + O$. The solid line with positive slope is the singlet state MEP; the solid line with negative slope is the triplet state MEP. The dashed lines are the singlet state energies at the triplet state geometries and vice versa. The dot near the center is the location of the lowest intersection of the singlet and triplet surfaces. The horizontal line represents the energy of the $NH_2 + OH$ asymptote.

energies for these simulations were obtained from direct CASPT2 evaluations employing the aug-cc-pvdz basis set. The active orbitals for these CASPT2 calculations consist solely of the radical orbitals of the two reacting fragments, and the CAS wave function is state averaged over the lowest degenerate states as necessary. Dynamical correction factors of 0.85 are applied, as suggested by the transition state recrossing observed in trajectory studies of related reactions.[31,32]

For the radical−radical reactions there are saddle points on the minimum energy path for the addition surface. These saddle points correlate with reorientations from those optimal at long-range to those optimal for chemical bonding. These reorientational saddle points occur at large enough separations that the variable reaction coordinate transition state theory approach should still be accurate. Interestingly, the interfragment vibrational frequencies at these saddle points are relatively large due to the small effective masses for NH, $NH_2$, and OH bending motions. Thus, one might expect quantum effects for these modes to be significant. However, sample evaluations of the quantum correction to the transition state partition function (based on evaluations of the quantum to classical harmonic numbers of states at these saddle points) indicate corrections of only about 5%.

For the complex forming reactions we have employed master equation simulations to examine the pressure dependence of the rate coefficients and the branching between the various channels. These master equation simulations employ exponential down energy transfer models and Lennard-Jones collision rates and are performed as described in refs 33 and 34. The predicted temperature dependent rate coefficients are fitted with modified Arrhenius expressions for the high and low pressure limits, while the Troe parameter[35,36] $F_{cent}$ is assumed to be temperature independent.

**Decomposition of $NH_2OH$ and Association of $NH_2$ with OH.** As discussed below, the experimental results for the decomposition of $NH_2OH$ show no evidence for the formation of $^3O$ atoms. This finding suggests that the rate of intersystem crossing from singlet $H_3NO$ to $NH_3 + {}^3O$ is much less than the decomposition rate. Thus, we consider only the decomposition to $NH_2 + OH$.

The isomerization of $NH_2OH$ to $H_3NO$ should be rapid relative to the dissociation rate, at least at low temperature or low pressure. Thus, the $H_3NO$ complex might be expected to contribute to the density of states for the complex. However,

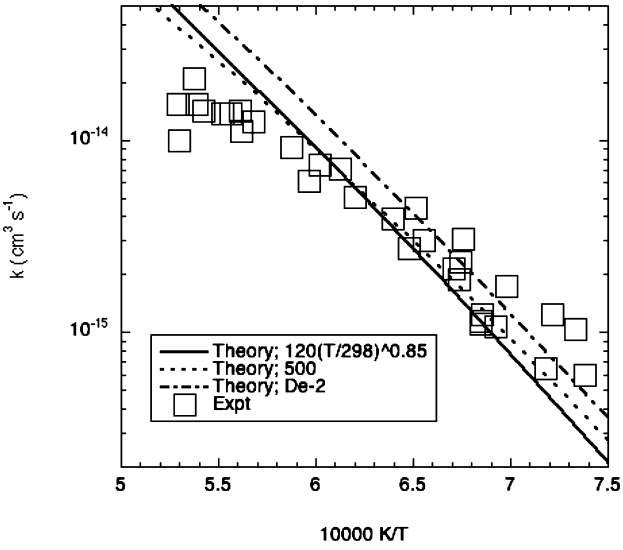


**Figure 4.** Arrhenius plot of the present experimental (symbols) and theoretical (lines) second-order rate coefficients for decomposition of $NH_2OH$. The solid and dot-dashed lines are for $\langle\Delta E_d\rangle$ values of $120(T/300)^{0.85}$ cm$^{-1}$, while the dotted line is for a constant $\langle\Delta E_d\rangle$ = 500 cm$^{-1}$. The dot-dashed line employs a dissociation energy that is 2 kcal/mol less than the CCSD(T)/CBS value.

sample calculations considering both the $NH_2OH$ and $H_3NO$ minima indicate that the density of states in the $H_3NO$ well is insignificant. Thus, the final results are for one-well simulations, where an accurate reduction from two-dimensions (total energy, $E$, and total angular momentum, $J$) to one dimension ($E$) is feasible.[33]

The master equation modeling of the kinetics requires some estimate of the average energy transferred. It is difficult to estimate this quantity from a priori theory. Instead most studies employ either a standard value or a fit to experiment and we follow that practice here. In prior studies the average downward energy transfer, $\langle\Delta E_d\rangle$, has been found to increase with temperature, with a proportionality of $T^{0.85}$ being fairly typical.[37−39] Here, the expression $120(T/300)^{0.85}$ cm$^{-1}$ for $\langle\Delta E_d\rangle$ yields theoretical second-order rate coefficients that reproduce the present experimental observations at the midpoint of the studied temperature range, as illustrated in Figure 4. Note that, according to the present theoretical analysis, the experimental observations are close to, but not quite in the low pressure limit. Thus, the theoretical predictions are reported for a pressure of 300 Torr, which is in the range of the experimental pressures.

While the above expression for $\langle\Delta E_d\rangle$ is fairly typical, it does yield a second-order rate coefficient that increases more rapidly with temperature than observed experimentally. Employing a constant $\langle\Delta E_d\rangle$ of 500 cm$^{-1}$ yields only slightly improved agreement, as also illustrated in Figure 4. Accurately reproducing the experimental temperature dependence via variations in solely $\langle\Delta E_d\rangle$ would require an $\langle\Delta E_d\rangle$ that decreases substantially with increasing temperature, which appears unphysical. Notably, decreasing the bond energy by 2 kcal/mol also yields only a modest improvement in the slope of the plot. Furthermore, the predicted bond energy of −61.7 kcal/mol is in good agreement with the Active Thermochemical Tables value of −62.0 (see Table 1).

Modified Arrhenius fits to the low and high pressure dissociation rate coefficients and the Troe parameter $F_{cent}$ are reported in Table 3 for $\langle\Delta E_d\rangle = 120(T/300)^{0.85}$ cm$^{-1}$. For completeness, a modified Arrhenius fit is also reported for the high pressure limit of the reverse association reaction. Fagerstrom et al.[40] have studied this association experimentally with pulse radiolysis combined with transient UV absorption spectroscopy and theoretically with the statistical adiabatic channel model (SACM).[41] The present predictions

**TABLE 3: Modified Arrhenius Fits to Theoretically Predicted Rate Coefficients for Reactions 1, and 5−12**

| reaction | rate | $A^a$ | $n$ | $E_a$ (K) | $T$ range (K) |
|---|---|---|---|---|---|
| $NH_2OH \rightarrow NH_2 + OH$ | $k_0$ | 9.05(13) | −5.96 | 33610 | 450−2500 |
| | $k_\infty$ | 1.40(20) | −1.31 | 32250 | 300−2500 |
| | $F_c$ | 0.35 | | | 450−2500 |
| $NH_2 + OH \rightarrow NH_2OH$ | $k_\infty$ | 4.95(−10) | −0.272 | −28 | 200−2500 |
| $NH_2 + OH \rightarrow {}^3NH + H_2O$ | $k$ | 4.71(−18) | 1.97 | −1130 | 300−2500 |
| ${}^3NH + H_2O \rightarrow NH_2 + OH$ | $k$ | 7.39(−18) | 2.05 | 11750 | 300−2500 |
| $NH_2 + OH \rightarrow NH_3 + {}^3O$ | $k$ | 6.18(−24) | 3.50 | −102 | 300−2500 |
| $NH_3 + {}^3O \rightarrow NH_2 + OH$ | $k$ | 4.63(−22) | 3.29 | 2250 | 300−2500 |
| $NH_2OH + OH \rightarrow HNOH + H_2O$ | $k$ | 2.55(−20) | 2.61 | −1780 | 300−2500 |
| $NH_2OH + OH \rightarrow H_2NO + H_2O$ | $k$ | 2.54(−19) | 2.28 | −652 | 300−2500 |
| $NH_2OH + NH_2 \rightarrow HNOH + NH_3$ | $k$ | 1.80(−25) | 4.00 | −49 | 300−2500 |
| $NH_2OH + NH_2 \rightarrow H_2NO + NH_3$ | $k$ | 1.57(−23) | 3.42 | −510 | 300−2500 |
| $NH_2OH + NH \rightarrow HNOH + NH_2$ | $k$ | 4.84(−27) | 4.40 | 787 | 400−2500 |
| $NH_2OH + NH \rightarrow H_2NO + NH_2$ | $k$ | 2.43(−27) | 4.60 | 1220 | 400−2500 |
| $NH + OH \rightarrow H_2O + {}^4N$ | $k_0$ | 2.64(−17) | 1.737 | −290 | 200−2500 |
| $NH + OH \rightarrow HNO + H$ | $k_0$ | 5.39(−10) | −0.376 | −23 | 200−2500 |
| $NH + NH \rightarrow HNNH$ | $k_\infty$ | 1.04(−10) | −0.036 | −81 | 200−2500 |
| $NH + NH \rightarrow N + NH_2$ | $k$ | 9.40(−25) | 3.88 | 172 | 300−2500 |
| $NH_2 + NH \rightarrow HNNH + H$ | $k_0$ | 7.07(−10) | −0.272 | −39 | 200−2500 |
| $NH_2 + NH \rightarrow N + NH_3$ | $k$ | 1.59(−20) | 2.46 | 54 | 200−2500 |
| $NH_2 + NH_2 \rightarrow H_2NNH_2$ | $k_0$ | 4.48(−14) | −5.49 | 1000 | 300−2500 |
| | $k_\infty$ | 9.33(−10) | −0.414 | 33 | 200−2500 |
| | $F_c$ | 0.31 | | | 200−2500 |
| $NH_2 + NH_2 \rightarrow HNNH + H_2$ | $k_0$ | 2.89(−16) | 1.02 | 5930 | 500−2250 |
| $NH_2 + NH_2 \rightarrow H_2NN + H_2$ | $k_0$ | 1.19(−19) | 1.88 | 4430 | 500−2250 |
| $NH_2 + NH_2 \rightarrow NH + NH_3$ | $k$ | 9.36(−24) | 3.53 | 278 | 300−2500 |
| $NH + NH_3 \rightarrow NH_2 + NH_2$ | $k$ | 8.53(−23) | 3.41 | 7350 | 300−2500 |

[a] Numbers in parentheses denote powers of ten. Rate coefficients are in units of cm, molecule, and s. $k = AT^n \exp(-E_a/T)$. The quantities $k_0$ and $k_\infty$ denote the low and high pressure limit rate coefficients, respectively, while $F_c$ denotes the Troe broadening parameter.

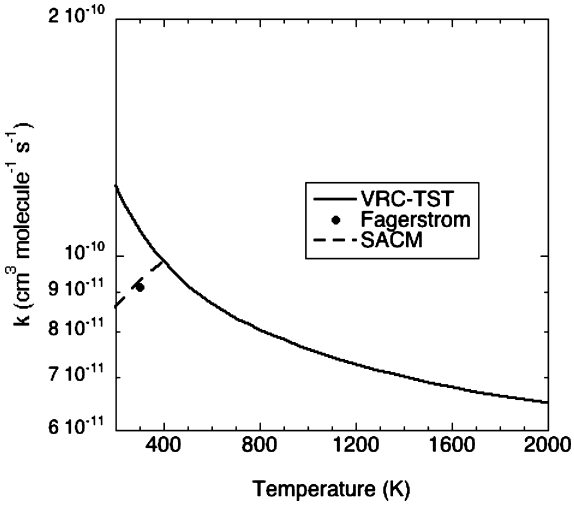


**Figure 5.** Arrhenius plot of the high pressure recombination rate coefficient for $NH_2 + OH$, where VRC-TST denotes the present calculations.

are compared with their data in Figure 5. Superficially, their experimental results, which were observed to be pressure independent, are in good agreement with the present predictions. However, our master equation simulations predict that their observations for pressures of 0.5−1 bar should be strongly into the falloff regime, being reduced by about an order of magnitude from the high pressure limit. A low energy decomposition to $NH_3 + O$ could explain this result but would be at odds with the observation of insufficient [O] in the present high temperature low pressure decomposition experiments. The qualitative difference between the present predictions and the SACM calculations is not particularly surprising given the empirical nature of the SACM calculations.

**$NH_2$ + OH Abstraction Reactions.** Reactions 5a and 5b are simple abstraction reactions having well-defined saddle points.

$$NH_2 + OH \rightarrow {}^3NH + H_2O \quad (5a)$$

$$NH_2 + OH \rightarrow NH_3 + {}^3O \quad (5b)$$

The rovibrational properties of the reactants and saddle points for reaction 5, as determined from CCSD(T)/CBS//CCSD(T)/aug-cc-pvdz calculations, are reported in Table 2.

The T1 diagnostic for the saddle points in each of these abstractions is large enough [(0.047) and (0.038) for (5a) and (5b), respectively] to imply significant multireference character and correspondingly increased uncertainties in the barrier heights and vibrational frequencies. A further indication of this uncertainty is provided by the difference in values obtained from calculations that employed spin-restricted, RCCSD(T), or unrestricted formalisms, UCCSD(T), and also for closely related RQCISD(T) and UQCISD(T) calculations. For reaction 5a, the RCCSD(T) and UQCISD(T) barrier heights differ by 1.5 kcal/mol, with the UQCISD(T) method providing the lowest barrier.

For these reasons, we have also undertaken both CASPT2 and CAS+1+2+QC calculations of these properties. The latter analyses employ an 8 electron 8 orbital CAS space, consisting of the NH and OH $\sigma,\sigma^*$ bonding pairs and the $NH_2$ and OH radical orbitals. The rovibrational analysis is performed for both the aug-cc-pvdz and aug-cc-pvtz basis sets with the CASPT2 method. CBS estimates are obtained from aug-cc-pvtz and aug-cc-pvqz results.

The CASPT2(8,8)/CBS//CASPT2/aug-cc-pvtz and CAS+1+2+QC(8,8)/CBS//CASPT2/aug-cc-pvtz predicted zero-point corrected barrier heights for channel 5a are 2.5 and 2.1 kcal/mol, and for channel 5b are 8.6 and 7.6 kcal/mol. The CAS+1+2+QC barrier heights are modestly greater than the UCCSD(T) ones of 1.7 and 6.1 kcal/mol, respectively.

The vibrational frequencies from the CASPT2(8,8) analysis are reported in Table 4. For the most part the differences between the CASPT2 and CCSD(T) frequencies are of only modest kinetic significance. However, the CASPT2 imaginary frequencies are considerably greater than the CCSD(T) ones, which implies significantly enhanced tunneling contributions. This enhanced tunneling contribution counteracts the effects of the increased barrier heights in the rate constant calculations.

In Figure 6 the predicted rate coefficient for reaction 5a is plotted versus temperature for calculations that employ (i) the CASPT2 frequencies and CAS+1+2+QC barrier height, (ii) the CCSD(T) vibrational frequencies and barrier height, or (iii) the CCSD(T) vibrational frequencies and a barrier height that is reduced by 2 kcal/mol from the CCSD(T)/CBS value. The only prior experimental studies of this reaction appear to be the indirect studies of Cheskis and Sarkisov[42] and of Kimball-Linne and Hanson.[43] The present theoretical predictions are markedly lower and cannot be reconciled with the room temperature estimate of $5 \times 10^{-11}$ cm$^3$ molecule$^{-1}$ s$^{-1}$ of Cheskis and Sarkisov. More significantly, the remarkably similar CASPT2 and CCSD(T) based theoretical estimates are each about a factor of 2−3 lower than the present experimental measurements and are also somewhat lower than the indirect measurements of ref 43. The empirical lowering of the CCSD(T) barrier by 2 kcal/mol yields reasonably satisfactory agreement with the two experimental results. The implied inaccuracy in the predicted barrier height is near the limit of its expected uncertainty.

Empirical estimates for the rate of reaction 5a have been presented in a number of modeling studies and data reviews[44−47] and the present unadjusted theory results are similar to most of

**TABLE 4: CASPT2(8,8) Stationary Point Frequencies[a] for $NH_2$ + OH Abstraction Reactions**

| | CASPT2 | |
|---|---|---|
| species | aug-cc-pvdz | aug-cc-pvtz |
| $NH_2 + OH$ | 3412, 3309, 1520, 3732 | 3444, 3347, 1533, 3760 |
| $^3NH + H_2O$ | 3909, 3788, 1639, 3187 | 3929, 3817, 1645, 3245 |
| $NH_3 + {}^3O$ | 3568, 3568, 3426 | 3587, 3587, 3455 |
| | 1645, 1645, 1076 | 1668, 1668, 1068 |
| $NH_2 + OH \rightarrow {}^3NH + H_2O$[b] | 3689, 3319, 1860, 1255, 735, 606, 340, *864i* | 3719, 3357, 1916, 1281, 744, 618, 347, *824i* |
| $NH_2 + OH \rightarrow NH_3 + {}^3O$ (A″) | 3562, 3418, 1597, 1414, 1272, 852, 492, 393, *1975i* | 3503, 3414, 1614, 1448, 1229, 848, 433, 377, *2336i* |

[a] Harmonic vibrational frequencies in cm$^{-1}$. [b] There is also one low frequency mode that is treated as a hindered rotor.

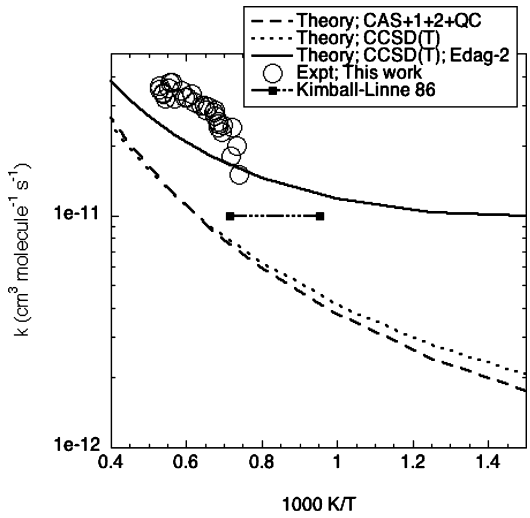


**Figure 6.** Arrhenius plot of the rate coefficient for the $NH_2 + OH \rightarrow {}^3NH + H_2O$ abstraction reaction. The dashed and dotted curves denote the theory predictions based on CAS+1+2+QC and CCSD(T) properties. The solid curve denotes CCSD(T) based predictions employing a barrier height reduced by 2 kcal/mol. The symbols denote past and present experimental results.

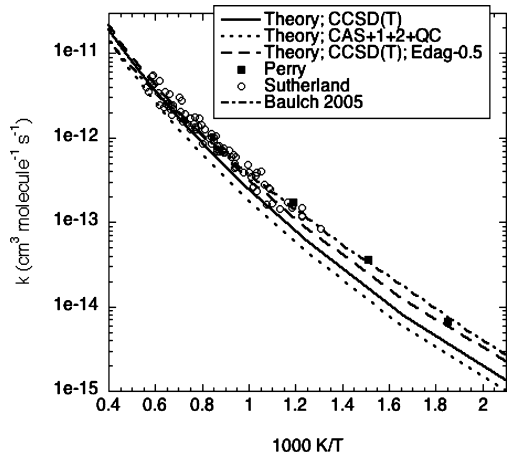


**Figure 8.** Arrhenius plot of the rate coefficient for the $NH_3 + {}^3O \rightarrow NH_2 + OH$ abstraction reaction. The solid and dotted lines denote the present CCSD(T) and CAS+1+2+QC based theory estimates, respectively. The dashed line denotes the present CCSD(T) results for a barrier that has been reduced by 0.5 kcal/mol. The symbols denote the two key experimental results, and the dashed-dotted line denotes the recent data review of Baulch et al.

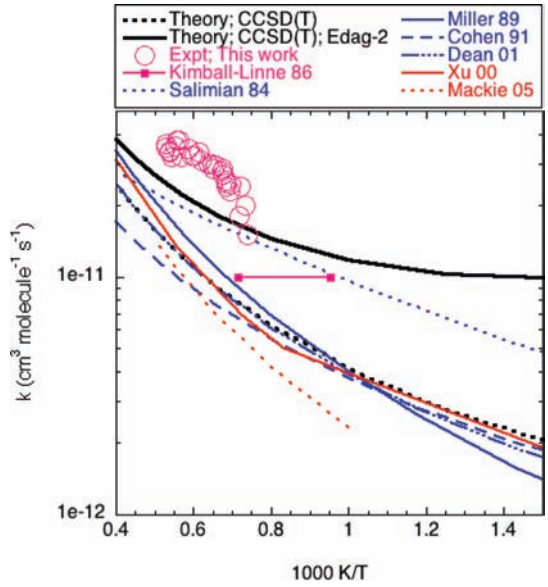


**Figure 7.** Arrhenius plot of the rate coefficient for the $NH_2 + OH \rightarrow {}^3NH + H_2O$ abstraction reaction. The black curves denote the present theory, the pink symobls denote present and prior experiment, the blue lines denote prior modeling, and the red denote prior theory. The solid line from the present theory denotes the predictions obtained when shifting the CCSD(T) barrier down by 2 kcal/mol, while the dashed line denotes the unadjusted CCSD(T) based predictions.

these estimates. Two related theoretical studies have also been presented.[9,48] These results are all compared with the present CCSD(T) based predictions in Figure 7. The canonical variational transition state theory study of Xu et al. employing small curvature tunneling and QCISD(T)/6-311G(d,p)//MP2/6-311G(d,p) energies is in good agreement with the present predictions. Meanwhile, the G3 based study of Mackie predicts significantly lower rate coefficients, perhaps due to the apparent neglect of tunneling.

There is also very limited experimental kinetic information for the reverse of reaction 5a, with the study of Rohrig and Wagner predicting a rate coefficient that is orders of magnitude greater than would be expected from the present theoretical analysis.[49] Notably, the CCSD(T) predicted 0 K exothermicity for reaction 5a is identical to that obtained with the Active Thermochemical Tables[50] analysis ($-25.43 \pm 0.05$ kcal/mol; see Table 1) employing the Core Thermochemical Network version 1.074.[51] Table 3 includes modified Arrhenius fits for reaction 5a in both the forward and reverse direction. These fits are to the predictions obtained with the CCSD(T) barrier adjusted down by 2 kcal/mol. The latter predictions provide a reasonable compromise between theory and experiment.

For the second abstraction channel, 5b, there is no experimental information. However, in this case, the reverse reaction has been quite widely studied and consensus values were suggested in the recent data evaluation of Baulch et al.[52] For completeness, we compare in Figure 8 the present theoretical predictions with only this data evaluation estimate and the two key experimental measurements of Sutherland et al.[53] and of Perry.[54] In making these predictions we have assumed that the rovibrational properties for the transition state in the excited electronic state are identical to those for the ground state.

For this reaction the CCSD(T) predictions are in reasonable agreement with the high temperature experimental results but modestly underpredict the lower temperature data. The CAS+1+2+QC results for reaction 5b are in slightly worse agreement with experiment, being modestly lower than the CCSD(T) predictions. Lowering the CCSD(T) barrier by 0.5 kcal/mol yields predictions that are in good agreement with experiment for the full range of temperature studied. The implied inaccuracy in the barrier heights is well within the error limits of the calculations. The CCSD(T) predicted 0 K reaction exothermicity for channel 5b of $-3.7$ kcal/mol similarly differs from the current Active Thermochemical Tables value ($-4.30 \pm 0.04$ kcal/mol) by 0.6 kcal/mol. Modified Arrhenius fits to the CCSD(T) theoretical predictions employing the adjusted barrier height are reported in Table 3 for reaction 5b and its reverse.

**$NH_2OH + X$; X = OH, $NH_2$, and NH Abstraction Reactions.** The reactions of $NH_2OH$ with OH, $NH_2$, and NH are also simple abstraction reactions having well-defined saddle points. Each of these radicals may abstract an H from either

the $NH_2$ or OH groups in $NH_2OH$, with the barriers to the former abstraction generally being lower.

$$NH_2OH + OH \rightarrow HNOH + H_2O \quad (6a)$$

$$\rightarrow NH_2O + H_2O \quad (6b)$$

$$NH_2OH + NH_2 \rightarrow HNOH + NH_3 \quad (7a)$$

$$\rightarrow NH_2O + NH_3 \quad (7b)$$

$$NH_2OH + NH \rightarrow HNOH + NH_2 \quad (8a)$$

$$\rightarrow NH_2O + NH_2 \quad (8b)$$

CCSD(T) calculations again indicate a significant degree of multireference character, with T1 diagnostics of about 0.04. Furthermore, CCSD(T)/aug-cc-pvdz vibrational analyses are moderately CPU intensive. Thus, the stationary point rovibrational properties reported in Table 5 are instead obtained from CASPT2/aug-cc-pvtz analyses. The active space for the CAS wave functions consisted of the NO $\sigma,\sigma^*$ bonding pair, the $\sigma,\sigma^*$ bonding pair for the H atom being abstracted, and the radical orbitals of the OH, $NH_2$, or NH coreactant. CCSD(T)/CBS and CASPT2/CBS barrier heights are obtained from singlet point evaluations at the CASPT2/aug-cc-pvtz geometries. The basis set extrapolations are based on calculations with either the aug-cc-pvtz and aug-cc-pvqz basis sets or the cc-pvtz and cc-pvqz basis sets.

The CCSD(T)/CBS based theoretical predictions of the rate coefficients for reaction 6 are illustrated in Figure 9. The dominant products are predicted to be $HNOH + H_2O$. These predictions slightly underestimate the value measured in the present experiments, with a decrease in the barrier heights by 1 kcal/mol yielding quantitative agreement. Calculations employing the CASPT2/CBS barrier height are instead about a factor of 2 lower than the CCSD(T)/CBS predictions in the experimentally studied temperature regime.

Although $NH_2$ is isoelectronic with OH, it is generally not as effective an abstracter. The weaker NH bonds result in higher abstraction barriers, with those for the abstraction from $NH_2OH$ being about 4 kcal/mol higher (cf. Table 5). These higher barriers lead to an overall abstraction rate for channels 7 that is a factor of 5 lower than for channels 6 at 1500 K. The predicted abstraction rate coefficients are within about 30% of those predicted by Dean and Bozzelli[47] over the key 1000−1500 K temperature range.

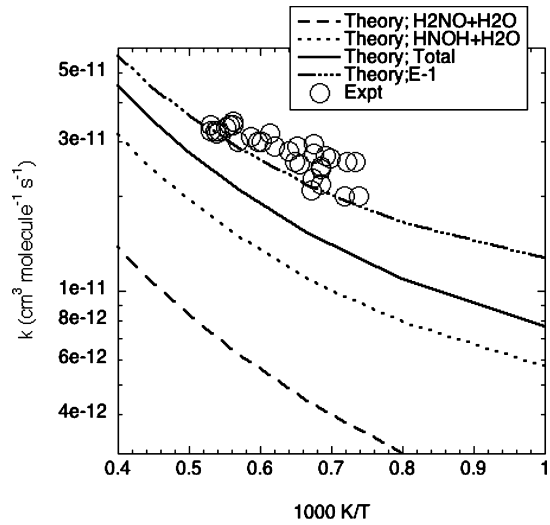


**Figure 9.** Arrhenius plot of the rate coefficients for the two abstraction reactions $NH_2OH + OH \rightarrow NH_2O + H_2O$ (dashed) and $NH_2OH + OH \rightarrow HNOH + H_2O$ (dotted) and their sum (solid). The dotted-dashed curve denotes the theory predictions for the total rate coefficient with barriers reduced by 1 kcal/mol from the CCSD(T)/CBS//CASPT2/aug-cc-pvtz values. The open circles denote the present experimental measurements.

NH is an even worse abstracter than $NH_2$, just as O atom is a worse abstracter than OH, due to the need to break their triplet couplings. Correspondingly, the abstraction barriers are another 6 kcal/mol higher and the total abstraction rate coefficient for channels 8 is a factor of 3 lower than for channels 7.

With these lower abstraction rates for the $NH_2$ and NH abstractions, it is unlikely that reactions 7 and 8 play a significant role in the $NH_2OH$ decomposition system. Nevertheless, for completeness, we report modified Arrhenius fitting parameters for reactions 6a, 6b, 7a, 7b, 8a, and 8b in Table 3. Those for reactions 6a and 6b are for the calculations which implement a lowering of the barrier by 1 kcal/mol.

**TABLE 5: Calculated Stationary Point Properties for $NH_2OH + X$ (X = OH, $NH_2$, and NH) Abstraction Reactions[a]**

| species | energy[b] | frequencies[c] | $B$[d] |
|---|---|---|---|
| $NH_2OH$ | | 3857, 3579, 3461, 1663, 1398, 1330, 1153, 912, 412 | 0.832, 0.832, 6.302 |
| OH | | 3782 | 18.7, 18.7 |
| $NH_2$ | | 3536, 3430, 1537 | 8.391, 13.01, 23.64 |
| NH | | 3375 | 16.8, 16.8 |
| $NH_2OH + OH \rightarrow HNOH + H_2O$ | −1.4 (1.1) | 3838, 3747, 3545, 1811, 1578, 1420, 1278, 935, 882, 790, 482, 324, 276, 147, *1527i* | 0.186, 0.221, 0.961 |
| $NH_2OH + OH \rightarrow H_2NO + H_2O$ | 0.8 (2.2) | 3707, 3603, 3497, 1667, 1597, 1328, 1188, 933, 809, 726, 620, 285, 192, 181, *2559i* | 0.195, 0.233, 1.007 |
| $NH_2OH + NH_2 \rightarrow HNOH + NH_3$ | 4.3 (4.5) | 3836, 3533, 3519, 3427, 1608, 1540, 1468, 1434, 1252, 942, 861, 752, 688, 496, 310, 167, 136, *2080i* | 0.175, 0.203, 0.951 |
| $NH_2OH + NH_2 \rightarrow H_2NO + NH_3$ | 3.9 (4.8) | 3583, 3532, 3466, 3430, 1659, 1556, 1414, 1329, 1161, 1139, 926, 798, 578, 540, 255, 165, 41, *2563i* | 0.171, 0.190, 1.095 |
| $NH_2OH + NH \rightarrow HNOH + NH_2$ | 10.9 (10.0) | 3823, 3409, 3384, 1527, 1425, 1407, 1238, 990, 849, 677, 517, 338, 151, 104, *2584i* | 0.182, 0.209, 1.029 |
| $NH_2OH + NH \rightarrow H_2NO + NH_2$ | 10.2 (10.1) | 3606, 3494, 3389, 1658, 1517, 1329, 1156, 911, 847, 767, 615, 319, 193, 74, *2811i* | 0.189, 0.219, 1.132 |

[a] Rovibrational properties are evaluated at the CASPT2/aug-cc-pvtz level. Energies are evaluated at the CASPT2/aug-cc-pvtz geometries with the CASPT2/CBS and CCSD(T)/CBS methods. For $NH_2OH$ the rovibrational properties reported are for the active space appropriate for the HNOH products. The rovibrational properties for reactions producing $H_2NO$ are slightly different due to different active spaces. [b] Zero point corrected energy in $cm^{-1}$ relative to $NH_2OH + X$; X = OH, $NH_2$, and NH. The first entry is the CCSD(T)/CBS energy, while the number in parentheses is the CASPT2/CBS energy. [c] Harmonic vibrational frequencies in $cm^{-1}$. [d] Rotational constants in $cm^{-1}$.

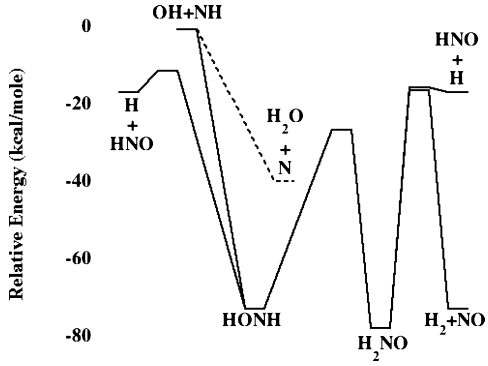


**Figure 10.** Schematic of calculated energies for the reaction of NH with OH. The solid lines correspond to the doublet state, while the dashed line corresponds to the quartet state.

**NH + OH Reactions.** The reaction of NH with OH can occur as either a direct abstraction on the quartet surface or an addition−elimination on the doublet surface.

$$NH + OH \rightarrow {}^4N + H_2O \quad (9a)$$

$$NH + OH \rightarrow HNOH \rightarrow \text{products} \quad (9b)$$

A schematic diagram of these reaction pathways is provided in Figure 10. The stationary point properties for reaction 9 were obtained from CCSD(T)/CBS//CCSD(T)/aug-cc-pvtz calculations, and are reported in Table 6. The basis set extrapolation is from aug-cc-pvqz and aug-cc-pvtz calculations. The reported energies are in good agreement with the corresponding Active Thermochemical Tables values (see Table 1), differing by at most 0.8 kcal/mol.

A related study of the $H_2NO$ potential energy surface was provided by Sumathi et al.[55] on the basis of a CCSD(T)6-311++G(3df,3pd)//CCSD(T)/6-311++G(d,p) theoretical analysis. The present larger basis sets coupled with the basis set extrapolation yields energies that range from 3 to 6 kcal/mol lower relative to NH + OH. Such deviations have significant implications for the kinetics.

The entrance channel for the addition−elimination reaction (9b) is treated with VRC-TST employing an analytic potential energy surface derived from a fit to CAS+1 + 2+QC/aug-cc-pvtz calculations. This analytic potential energy surface will be described in greater detail in a separate publication that includes a detailed comparison of quantum dynamics and VRC-TST for this addition reaction. The overall reaction rate for (9b) is evaluated with a master equation formalism that includes separate transition state theory treatments for each of the processes illustrated in Figure 10. This formalism is implemented in the low pressure limit and includes a proper treatment of the conservation of energy and total angular momentum.

Sample master equation simulations indicate that for pressures of 100 atm or lower the addition−elimination process is effectively in its collisionless limit. These master equation simulations also indicate that the dominant products are HNO + H, with NO + $H_2$ contributing only about 5%. Furthermore, as illustrated in Figure 11, there is a modest deviation of this collisionless limit rate coefficient from the high pressure limit, particularly at high *T*. The predictions are in good agreement with the one experimental study of Hack and Kurzke[56] at room temperature. The estimate from the modeling study of Miller and Bowman[45] is in reasonable agreement with the present predictions, especially for temperatures of 1000−2000 K, as is the theoretical estimate of Sumathi et al.[55] However, the latter study also predicts a roughly equal branching between NO + $H_2$ and HNO + H, in sharp contrast with the present predictions.

The present predictions for the abstraction rate are also illustrated in Figure 11, along with some key modeling estimates. Again, there do not appear to be any direct experimental measurements. Hansen's modeling estimate,[44] which is also employed in the Miller Bowman study,[45] is in the best agreement with our calculations. The other estimates are also within a factor of 2−3 of our prediction, with that of Cohen[46] being higher, while that of Dean is lower.[47]

A quartet abstraction to produce $NH_2$ + O is also possible but lies at considerably higher energy, as reported in Table 6. Furthermore, the formation of $NH_2$ + O on the doublet surface via addition elimination is expected to dominate over the quartet abstraction since the reverse process on the doublet surface proceeds via the barrierless formation of $H_2NO$.

Modified Arrhenius fits to the theoretical predictions for the rate coefficients for reactions 9a and 9b are provided in Table 3.

**NH + NH Reaction.** The reaction of NH with NH also proceeds via either direct abstraction or addition followed by elimination of either an H atom or $H_2$ molecule:

$$NH + NH \rightarrow N + NH_2 \quad \text{(triplet surface)} \quad (10at)$$

$$NH + NH \rightarrow N + NH_2 \quad \text{(quintet surface)} \quad (10aq)$$

$$NH + NH \rightarrow HNNH \rightarrow NNH + H \quad \text{(singlet surface)} \quad (10bs)$$

$$NH + NH \rightarrow HNNH \rightarrow NNH + H \quad \text{(triplet surface)} \quad (10bt)$$

$$NH + NH \rightarrow HNNH \rightarrow N_2 + H_2 \quad \text{(singlet surface)} \quad (10cs)$$

A schematic diagram of these reaction pathways is provided in Figure 12. Aside from the triplet abstraction (10at), the stationary point properties for reactions 10aq−cs were obtained from CCSD(T)/CBS//CCSD(T)/aug-cc-pvtz calculations, and are reported in Table 7. Again there is good agreement with the Active Thermochemical Tables values reported in Table 1, with a maximum difference of 0.6 kcal/mol. For the triplet abstraction, there was a very large T1 diagnostic of 0.08, and the properties were instead obtained from CASPT2 calculations with an 8 electron 8 orbital active space consisting of the NH radical and NH $\sigma,\sigma^*$ orbitals. Smaller, but still significant T1 diagnostics of 0.035 and 0.040 were encountered for the singlet and triplet states of HNNH.

The abstraction occurs with a significant barrier on either a triplet or a quintet surface, while the addition occurs barrierlessly on either a singlet or triplet surface. Thus, the addition process is expected to dominate the kinetics. H loss from HNNH occurs without a reverse barrier on the singlet surface and only a modest barrier on the triplet surface. Furthermore, the NNH + H products lie well below the saddle point for $H_2$ loss on the singlet surface. Thus, channel 10bs should dominate over (10cs). Nevertheless, there may be a modest amount of $H_2$ product formed via a roaming mechanism[57] in which the H atom abstracts another H atom from the NNH fragment during its dissociation. An exploration of this channel was deemed beyond the scope of the present work.

The large exothermicity for the NNH + H channel, coupled with the low activation energy for dissociation of NNH, implies that the products of reactions 10bs and 10bt, NNH + H, are better considered as $N_2$ + H + H. In particular, the initial NNH

**TABLE 6: Calculated CCSD(T)/CBS//CCSD(T)/aug-cc-pvtz Stationary Point Properties for the NH + OH System**

| species | energy[a] (kcal/mol) | frequencies ($cm^{-1}$) | rotational constants ($cm^{-1}$) |
|---|---|---|---|
| OH + NH | | 3718 | 18.77, 18.77 |
| | | 3264 | 16.59, 16.59 |
| N + $H_2O$ | −39.2 | 3920, 3811, 1646 | 9.444, 14.53, 26.98 |
| HNO + H | −16.3 | 2948, 1589, 1532 | 1.304, 1.401, 18.73 |
| $H_2$ + NO | −72.2 | 4401 | 60.56, 60.56 |
| | | 1894 | 1.687, 1.687 |
| $NH_2$ + O | 9.8 | 3453, 3360, 1539 | 8.324, 12.95, 23.30 |
| HNOH | −70.2 | 3785, 3373, 1574 | 0.953, 1.054, 9.941 |
| | | 1270, 1088, 735 | |
| $H_2NO$ | −77.2 | 3693, 3417, 1527 | 1.032, 1.136, 10.61 |
| | | 1428, 1355, 399 | |
| NH + OH → N + $H_2O$ | 0.8 | 3724, 2504, 664 | 0.297, 0.302, 18.59 |
| | | 455, 341, *265i* | |
| NH + OH → $NH_2$ + O (A″) | 15.3 | 3348, 1442, 868 | 0.366, 0.375, 16.08 |
| | | 585, 392, *1632i* | |
| NH + OH → $NH_2$ + O (A′) | 15.9 | 3414, 1430, 878 | 0.370, 0.379, 15.47 |
| | | 645, 387, *1738i* | |
| $H_2NO$ → HNOH | −25.9 | 3385, 2599, 1421 | 0.956, 1.016, 9.227 |
| | | 1234, 981, *2022i* | |
| $H_2NO$ → HNO + H | −14.9 | 2966, 1573, 1513 | 0.905, 1.040, 4.496 |
| | | 361, 216, *517i* | |
| HNOH → HNO + H | −10.6 | 2599, 1531, 1365 | 0.989, 1.154, 5.403 |
| | | 819, 326, *2893i* | |
| $H_2NO$ → NO + $H_2$ | −15.8 | 2386, 1437, 1123 | 1.059, 1.166, 6.961 |
| | | 1100, 798, *1826i* | |

[a] Zero point corrected energy relative to NH + OH.

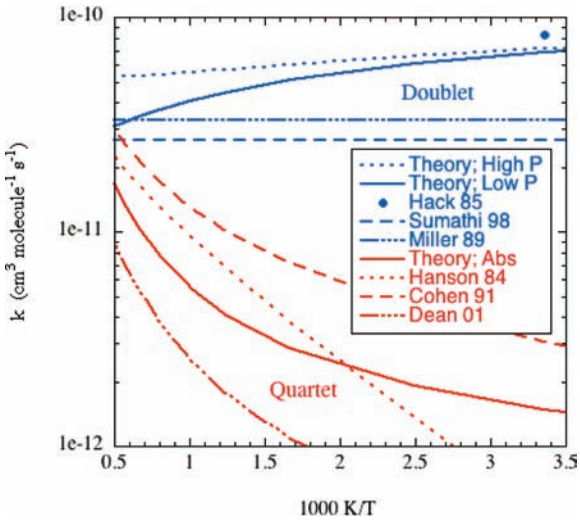


**Figure 11.** Arrhenius plot of the rate coefficients for the reactions NH + OH → HNO + H (in blue) and NH + OH → N + $H_2O$ (in red).

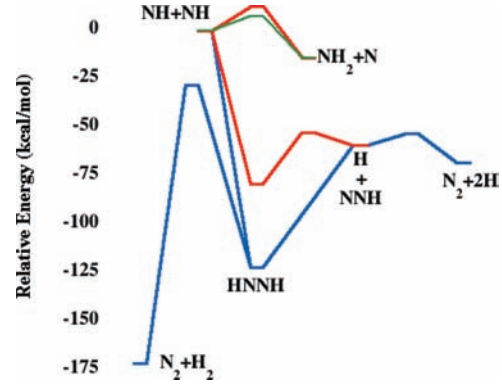


**Figure 12.** Schematic of calculated energies for the reaction of NH with NH. The blue, red, and green lines correspond to the singlet, triplet, and quintet states, respectively.

formed would be expected to predominantly have an internal energy that exceeds its dissociation threshold and thus will dissociate collisionlessly. This large exothermicity also implies that there is unlikely to be any significant stabilization of HNNH on either the singlet or triplet potentials and sample master equation simulations verify this expectation. Thus, our calculation of the rate for channels 10bs and 10bt focuses on the singlet and triplet addition reactions. Note that the corresponding quintet surface for addition is repulsive.

The rate coefficient for each of the additions [(10bs) + (10bt)] is predicted by direct variable-reaction-coordinate transition state theory. The temperature dependence of the predicted total addition rate coefficient is plotted in Figure 13 together with the limited available experimental data.[58−61] The predictions are in remarkably good agreement with the shock tube experimental data of Mertens et al.,[58] while the remaining data are somewhat discordant. The estimate from the classic Miller and Bowman $NO_x$ modeling study[45] is about a factor of 2 lower than the present prediction. A modified Arrhenius fit to the theoretical predictions for the high pressure addition rate is reported in Table 3. This rate coefficient should correspond to that for production of both $N_2$ + H + H and $N_2$ + $H_2$. The former products are expected to be the dominant channel with a branching fraction of about 0.9 ± 0.1.

For the abstraction reactions on the quintet and triplet surfaces the total rate coefficient is only $5 \times 10^{-12}$ $cm^3$ $molecule^{-1}$ $s^{-1}$ at 2000 K, which is only 6% of the addition elimination rate coefficient. For temperatures of 2500 K and lower the triplet state makes only a minor contribution due to its greater barrier. The parameters of a modified Arrhenius fit to the sum of the abstraction rate coefficients are reported in Table 3.

There do not appear to be any prior experimental studies of the abstraction reactions. However, the abstraction on the quintet surface was previously studied theoretically by Xu et al.[62] with UMP2 stationary point analyses and UMP-SAC4

**TABLE 7: Calculated CCSD(T)/CBS//CCSD(T)/aug-cc-pvtz Stationary Point Properties for the NH + NH System**

| species | energy[a] (kcal/mol) | frequencies ($cm^{-1}$) | rotational constants ($cm^{-1}$) |
|---|---|---|---|
| NH + NH | | 3264 | 16.59, 16.59 |
| | | 3264 | 16.59, 16.59 |
| NNH + H | −59.1 | 2901, 1806, 1104 | 1.434, 1.535, 21.90 |
| $N_2 + H_2$ | −171.3 | 2339 | 1.974, 1.974 |
| | | 4401 | 60.56, 60.56 |
| $N_2 + H + H$ | −68.0 | 2339 | 1.974, 1.974 |
| $N + NH_2$ | −13.9 | 3454, 3360, 1540 | 8.324, 12.95, 23.30 |
| HNNH | −122.1 | 3297, 3267, 1612 | 1.150, 1.299, 10.04 |
| | | 1552, 1344, 1318 | |
| $^3$HNNH | −79.0 | 3328, 3305, 1428 | 1.136, 1.151, 11.31 |
| | | 1041, 1032, 763 | |
| $^3$HNNH → NNH + H | −52.3 | 3022, 1720, 1104 | 1.101, 1.175, 6.811 |
| | | 698, 493, *1111i* | |
| $N_2H + H \rightarrow N_2 + H + H$ | −52.9 | 2098, 735, *1600i* | 1.409, 1.583, 12.82 |
| $NH + NH \rightarrow N + NH_2$ | 7.0 | 3292, 1146, 751 | 0.347, 0.354, 16.66 |
| quintet surface | | 660, 482, *2214i* | |
| $NH + NH \rightarrow N + NH_2$ | 12.1 | 3266, 1082, 675 | 0.357, 0.365, 16.42 |
| triplet surface[b] | | 463, 400, *2242i* | |
| HNNH → $N_2 + H_2$ | −27.8 | 2269, 1624, 1127 | 1.135, 1.411, 5.793 |
| | | 885, 773, *3129i* | |

[a] Zero point corrected energy relative to NH + NH. [b] Caclulated relative to quintet abstraction transition state with PT2(8e,8o)/CBS//PT2(8e,8o)/aug-cc-pvtz and added to triplet transition state energy.

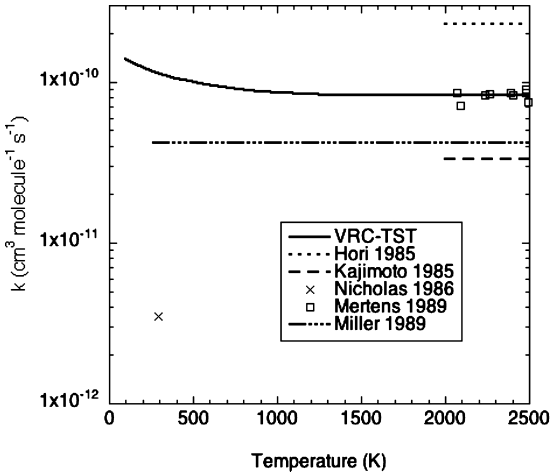


**Figure 13.** Arrhenius plot of the rate coefficient for the addition reaction of NH with NH.

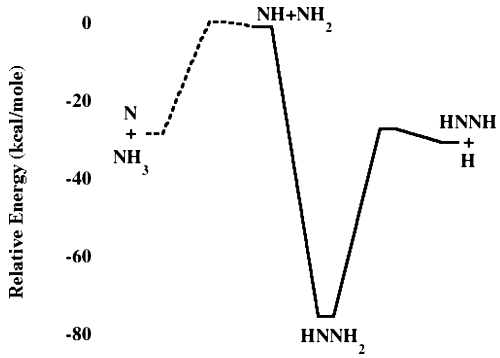


**Figure 14.** Schematic of calculated energies for the reaction of NH with $NH_2$. The solid and dashed lines correspond to the doublet and quartet states, respectively.

energy calculations. Their predicted rate coefficient is significantly greater, being about a factor of 4 larger at 1000 K, due in large part to a lower prediction for the barrier height of 6.4 versus 7.5 kcal/mol. The present predictions are expected to be more accurate due to the use of higher accuracy ab initio electronic structure methods.

**NH + $NH_2$ Reaction.** The reaction of NH with $NH_2$ also proceeds via either addition (on the doublet surface) followed by elimination of an H atom or abstraction (on the quartet surface):

$$NH + NH_2 \rightarrow HNNH_2 \rightarrow HNNH + H \qquad (11a)$$

$$NH + NH_2 \rightarrow N + NH_3 \qquad (11b)$$

A schematic diagram of these reaction pathways is provided in Figure 14, and the corresponding CCSD(T)/CBS//CCSD(T)/aug-cc-pvdz energies are reported in Table 8. For this reaction the maximum deviation from the Active Thermochemical Tables values reported in Table 1 is only 0.3 kcal/mol. A transition state for elimination of $H_2$ from $HNNH_2$ is likely to exist but was not found here. Regardless, such a transition state is expected to again lie higher in energy and have less entropy than that for H loss and thus should not make a significant contribution to the kinetics.

The barrierless nature of the initial addition coupled with the modest barrier to abstraction suggests that addition should again dominate over abstraction. Furthermore, the large exothermicity for channel 11a, the small reverse barrier, and the small molecular size together suggest that under most conditions there should be little stabilization. Sample master equation simulations verify that there is indeed little stabilization, but they also indicate that at the higher temperatures there is some minor back dissociation to reactants.

The VRC-TST predictions for the high pressure addition and low pressure bimolecular rate coefficients are plotted versus temperature in Figure 15 together with the available experimental data.[63−66] The theoretical predictions are in satisfactory agreement with the experimental results, being within the experimental error bars of all but the very recent experimental study of Bahng and Macdonald.[63] The estimate of Miller and Bowman[45] is also in good agreement with the present theoretical prediction.

A modified Arrhenius fit to the predicted abstraction rate coefficient is reported in Table 3. There are two commonly

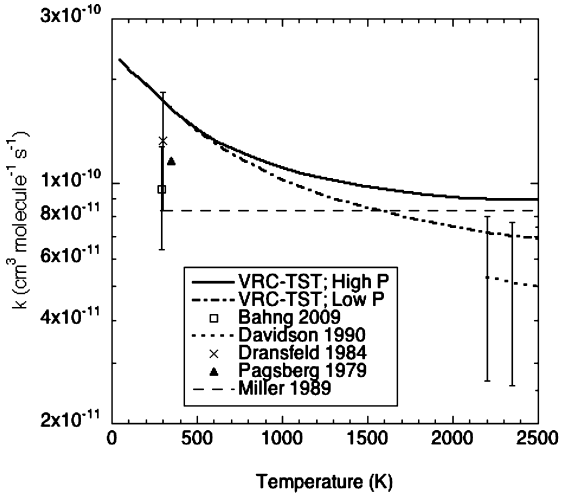


**Figure 15.** Arrhenius plot of the rate coefficient for the reaction of NH with $NH_2$ on the doublet surface; channel 11a. The solid and dot-dashed lines correspond to the high pressure and collisionless limit of the present VRC-TST calculations. The symbols and the dashed lines correspond to the various experimental measurements.

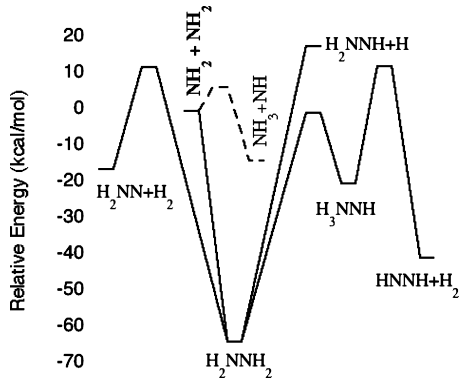


**Figure 16.** Schematic of calculated energies for the reaction of $NH_2$ with $NH_2$. The solid and dashed lines correspond to the singlet and triplet states, respectively.

employed empirical estimates for reaction 11b. The present predictions are essentially identical to the empirical estimate of Dean and Bozelli,[47] which are about an order of magnitude greater than that of Salimian et al.[67] There do not appear to be any experimental studies of the abstraction reaction.

**$NH_2 + NH_2$ Reaction.** The reaction of $NH_2$ with $NH_2$ also proceeds via either addition (on the singlet surface) followed by elimination of either $H_2$ or an H atom or abstraction (on the triplet surface):

$$NH_2 + NH_2 \rightarrow H_2NNH_2 \rightarrow H_2NN + H_2 \quad (12a)$$

$$NH_2 + NH_2 \rightarrow H_2NNH_2 \rightarrow HNNH + H_2 \quad (12b)$$

$$NH_2 + NH_2 \rightarrow H_2NNH_2 \rightarrow H_2NNH + H \quad (12c)$$

$$NH_2 + NH_2 \rightarrow NH + NH_3 \quad (12d)$$

A schematic diagram of these reaction pathways is provided in Figure 16, and the corresponding CCSD(T)/CBS//CCSD(T)/aug-cc-pvdz energies are reported in Table 9. For this reaction the maximum deviation from the Active Thermochemical Tables values reported in Table 1 is only 0.4 kcal/mol. The G2M(MP2) energies from an earlier theoretical analysis of Hwang and Mebel[68] are also reported in Table 9.

For the abstraction reaction 12d there is a relatively modest T1 diagnostic of 0.033. Nevertheless, we have performed a CASPT2(4e,4o) analysis, which yields a saddle point energy of 5.2 kcal/mol in reasonable agreement with the CCSD(T) value of 6.6 kcal/mol. An earlier theoretical study of Xu et al.[69] found zero-point corrected barriers of 6.9, 5.8, 2.3, and 3.7 at the UMP4/6-311G(d,p), UQCISD(T)/6-311G(d,p), G1, and UMP-SAC4/6-311G(d,p) levels each at the UMP2/6-311G(d,p) geometries. The present CCSD(T) based predictions for the abstraction rate are reported in Table 3. The high temperature experimental study of Davidson et al. is in reasonable agreement with these predictions, being about 1.5 times greater over the studied range of 2200−2800 K.[64] The predicted rate coefficients are also quite similar to the earlier predictions of Xu et al.,[69] being slightly lower at low temperature and slightly higher at high temperature, but always being within about 50%.

Wagner and co-workers provided a more direct experimental study of the related reverse abstraction reaction (−12d).[70] The corresponding CCSD(T) based theoretical predictions are reported in Table 3. As illustrated in Figure 17, these theoretical predictions for the reverse abstraction are within about 50% of the measured values.

The present dynamically corrected VRC-TST predictions for the high pressure recombination to form $H_2NNH_2$ are illustrated in Figure 18. These predictions provide a reasonable representation of the somewhat disparate experimental measurements.[40,71−75]

The pressure dependence of the recombination reaction was recently studied at room temperature by Bahng and Macdonald.[76] The rate coefficients obtained in this study for pressures in the 2−10 Torr range are about an order of magnitude larger than those obtained in the earlier study of Khe and co-workers.[73] A master equation fit to the data from Bahng

**TABLE 8: Calculated CCSD(T)/CBS//CCSD(T)/aug-cc-pvdz Stationary Point Properties for the NH + $NH_2$ System**

| species | energy[a] (kcal/mol) | frequencies ($cm^{-1}$) | rotational constants ($cm^{-1}$) |
|---|---|---|---|
| $NH + NH_2$ | | 3213 | 16.21, 16.21 |
| | | 3418, 3320, 1527 | 8.169, 12.80, 22.58 |
| HNNH + H | −29.6 | 3263, 3233, 1604 | 1.128, 1.275, 9.799 |
| | | 1547, 1334, 1305 | |
| $N + NH_3$ | −27.5 | 3631, 3622, 3464 | 6.055, 9.853, 10.11 |
| | | 1648, 1634, 902 | |
| $HNNH_2$ | −74.4 | 3624, 3475, 3378, 1649 | 0.887, 1.002, 6.613 |
| | | 1478, 1216, 1138, 712, 603 | |
| $HNNH_2 \rightarrow HNNH + H$ | −26.3 | 3286, 3256, 1580, 1494 | 0.890, 1.002, 4.147 |
| | | 1321, 1270, 412, 338, *855i* | |
| $NH + NH_2 \rightarrow N + NH_3$ | 1.2 | 3425, 3326, 1520, 1008 | 0.319, 0.323, 9.202 |
| | | 989, 903, 475, 442, *1091i* | |

[a] Zero point corrected energy relative to $NH + NH_2$.

**TABLE 9: Calculated CCSD(T)/CBS//CCSD(T)/aug-cc-pvdz Stationary Point Properties for the $NH_2 + NH_2$ System**

| species | energy[a] (kcal/mol) | frequencies ($cm^{-1}$) | rotational constants ($cm^{-1}$) |
|---|---|---|---|
| $NH_2 + NH_2$ | | 3418, 3320, 1527 | 8.169, 12.80, 22.58 |
| | | 3418, 3320, 1527 | 8.169, 12.80, 22.58 |
| $NH_3 + NH$ | −13.6 | 3213, 3631, 3622, 3464 | 6.055, 9.853, 10.11 |
| | [−14.3] | 1648, 1634, 902 | 16.21, 16.21 |
| $H_2NN + H_2$ | −16.6 | 4344, 3113, 3097, 1719 | 1.129, 1.259, 10.99 |
| | [−19.8] | 1572, 1308, 983 | 57.62, 57.62 |
| $HNNH + H_2$ | −40.6 | 4344, 3197, 3109, 1554 | 1.128, 1.275, 9.799 |
| | [−44.4] | 1535, 1352, 1231 | 57.62, 57.62 |
| $H_2NNH + H$ | 17.8 | 3624, 3475, 3378, 1649, 1478 | 0.887, 1.002, 6.613 |
| | | 1216, 1138, 712, 603 | |
| $H_2NNH_2$ | −63.7 | 3426, 1665, 1652, 1332, 1292 | 0.793, 0.793, 4.679 |
| | [−62.8] | 1105, 1027, 842, 404 | |
| $H_3NNH$ | −20.1 | 3513, 3353, 3335, 3291, 1655, 1640 | 0.751, 0.783, 4.552 |
| | [−21.9] | 1470, 1430,1014, 987, 775, 344 | |
| $H_2NNH_2 \rightarrow H_2NN + H_2$ | 12.0 | 3557, 3437, 2523, 1683, 1332, 1282 | 0.802, 0.844, 3.645 |
| | [10.9] | 1232, 1041, 824, 587, 315, *1511i* | |
| $H_2NNH_2 \rightarrow H_3NNH$ | −0.6 | 3661, 3527, 3354, 2643, 1551, 1443 | 0.654, 0.686, 4.605 |
| | [−2.3] | 1326, 910, 857, 578, 350, *1514i* | |
| $H_3NNH \rightarrow HNNH + H_2$ | 12.3 | 3523, 3370, 3080, 1599, 1477, 1311 | 0.741, 0.785, 3.542 |
| | [13.1] | 1131, 834, 581, 471, 253, *608i* | |
| $NH_2 + NH_2 \rightarrow NH + NH_3$ | 6.6 | 3446, 3347, 3307, 1538, 1421, 1200 | 0.330, 0.333, 5.392 |
| | (5.2)[b] | 860, 761, 512, 417, 100, *1961i* | |

[a] Zero point corrected energy relative to $NH_2 + NH_2$. The primary entries are the present CCSD(T)/CBS//CCSD(T)/aug-cc-pvdz values, while the numbers in square brackets are the G2M results from ref 68. [b] These calculations are done with the CASPT2(4e,4o) method rather than CCSD(T).

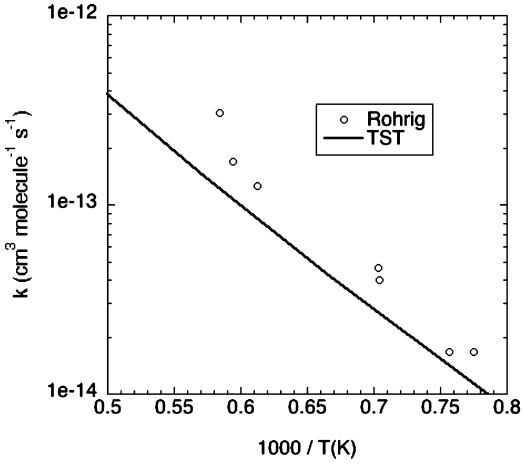


**Figure 17.** Plot of the rate coefficient for the reaction of NH with $NH_3$ on the triplet surface; channel (−12d). The solid line denotes the present TST calculations and the symbols denote the experimental measurements of Rohrig et al.

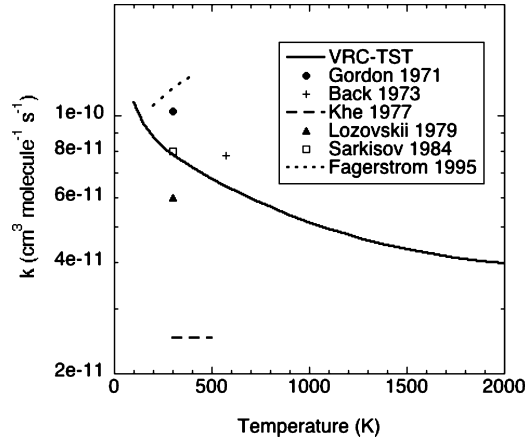


**Figure 18.** Plot of the high pressure recombination rate coefficient for $NH_2 + NH_2$. The solid line denotes the present VRC-TST calculations, while the symbols and dashed and dotted lines denote various experimental results.

and Macdonald for $N_2$ bath gas requires a $\langle \Delta E_d \rangle$ value of ~1000 $cm^{-1}$. In contrast, fitting the data of Khe et al. requires a $\langle \Delta E_d \rangle$ of less than 80 $cm^{-1}$. The former value for $\langle \Delta E_d \rangle$ is substantially larger than typical of fits for other systems, while the latter value is close to but somewhat smaller than typical. Given the uncertainty in the accuracy of these two sets of data, we have simply chosen to employ a compromise of $150(T/300)^{0.85}$ $cm^{-1}$ in making more global predictions for the pressure dependence. Interestingly, this form yields results that provide a reasonable reproduction of the higher pressure data of Lozovskii et al.[74] The Troe fit to master equation results with this form are reported in Table 3.

The larger rate coefficients found by Bahng and Macdonald may be indicative of some enhanced energy transfer process and suggest the need for further study of this system. Note that the full master equation prediction for the rate coefficient already deviates by about a factor of 4 from the $k_0 P$ limit in the 2−10 Torr range. As a result, the $k_0$ value reported in Table 3 for this recombination of $3.9 \times 10^{-29}$ $cm^6$ $molecule^{-2}$ $s^{-1}$ at $T = 300$ K is accidentally quite close to the value of $5.7 \times 10^{-29}$ $cm^6$ $molecule^{-2}$ $s^{-1}$ obtained by Bahng and Macdonald from a linear fit at their studied pressures.

The predicted low pressure rate coefficients for channels 12a and 12b are also reported in Table 3. These values are always much lower than the abstraction rate coefficient and so are essentially irrelevant to the kinetics. Note, however, that the experiments of Stothard et al.[77] measure a room temperature rate coefficient for these channels of $(1.3 \pm 0.5) \times 10^{-12}$ $cm^3$ $molecule^{-1}$ $s^{-1}$, which is $10^8$ times greater than our prediction. Notably, these experiments do show a strong sensitivity to various secondary reactions including the source reaction, $F + NH_3$, and wall reactions. The rate coefficient for channel 12c is also not expected to be significant for all but very high temperatures due to its reasonably large endothermicity.

## Experiment

**Methods.** The present experiments were performed with the reflected shock tube technique using both O-atom atomic resonance absorption spectrometry (ARAS) and OH-radical electronic absorption detection. The methods and the apparatus currently being used have been previously described,[78,79] and only a brief description of the experiment will be presented here.

For the O-atom experiments, the shock tube was fabricated from a 7 m (10.2 cm o.d.) 304 stainless steel tube; however, for the OH-radical experiments, it was constructed from 304 stainless steel in three sections. The 10.2 cm o.d. cylindrical sections were separated from the He driver chamber by a 4 mil unscored 1100-H18 aluminum diaphragm, but for the OH apparatus, a 0.25 m transition section then connects the first and third sections. The third section was of rounded corner (radius, 1.71 cm) square design and was fabricated from flat stock (3 mm) with a mirror finish. In both configurations, the tubes were routinely pumped between experiments to less than $10^{-8}$ Torr by an Edwards Vacuum Products Model CR100P packaged pumping system. Shock wave velocities were measured with eight equally spaced pressure transducers (PCB Piezotronics, Inc., Model 113A21) mounted along the downstream part of the test section and recorded with a 4094C Nicolet digital oscilloscope. Temperature and density in the reflected shock wave regime were calculated from this velocity. This procedure has been given previously, and corrections for boundary layer perturbations have been applied.[80−82] The oscilloscope was triggered by pulses derived from the last velocity gauge signal. In both cases, the photometer systems were radially located at 6 cm from the end plate.

For O-atom detection, the windows were crystalline $MgF_2$, and the resonance lamp beam intensity was measured by an EMR G14 solar blind photomultiplier tube and recorded with an oscilloscope as described previously.[83,84] For the OH-radical experiments, a White cell, as described previously,[3,4,85] was used to increase the absorption path length. The White cell was constructed from two flat fused silica windows (3.81 cm), mounted on the tube across from one another, with broad-band antireflection (BB AR) coating for UV light. The distance between windows was 8.745 cm. The optical configuration consisted of an OH resonance lamp,[4,85] multipass reflectors, an interference filter at 308 nm, and a photomultiplier tube (1P28) all mounted external to the shock tube. At the entrance to the multipass cell, OH resonance radiation was collimated with a set of lenses and was focused onto the reflector on the opposite side of the shock tube through two AR coated windows that were flush mounted to the inside of the shock tube. The reflectors and windows were obtained from the CVI Laser Corporation. These reflectors were attached to adjustable mounts, and the center points of windows and mirrors were all in a coaxial position. With this new configuration, multiple passes were used, thereby amplifying the measured absorbances by about a factor of 5 over that used in the previous work.[4,85] This increase in sensitivity for OH-radical detection allows for the detection of lower [OH] and therefore decreases the importance of secondary reaction perturbations.

**Gases.** High purity He (99.995%), used as the driver gas, was from AGA Gases. Scientific grade Kr (99.999%), the diluent gas in reactant mixtures, was from Spectra Gases, Inc. The ~10 ppm impurities ($N_2$, 2 ppm; $O_2$, 0.5 ppm; Ar, 2 ppm; $CO_2$, 0.5 ppm; $H_2$, 0.5 ppm; $CH_4$, 0.5 ppm; $H_2O$, 0.5 ppm; Xe, 5 ppm; $CF_4$, 0.5 ppm) either are all inert or are in sufficiently low concentration so as to not perturb either O-atom or OH-radical profiles. The microwave driven resonance lamp operated at 50 W and 1.8 Torr He with a trace of $O_2$ (research grade (99.999%) from MG Industries) added to give $X_{O_2} = 1 \times 10^{-3}$. The microwave driven OH lamp operated at ~25 Torr. Distilled water, evaporated at one atmosphere into ultrahigh purity grade Ar (99.999%) from AGA Gases, was used in the resonance lamp. A 99.999% pure water solution of hydroxylamine, $NH_2OH$ (50% by weight) from Sigma Aldrich Chemical Co. Inc. was thoroughly outgassed and was used to prepare mixtures. It was impossible to completely separate the two components by distillation. The [$NH_2OH$] present in the final mixtures was determined by shock heating mixtures at high-$T$ and quantitatively observing $[OH]_{max}$ since the predominant dissociation products were expected to be $NH_2$ + OH. We found that we could deliver (9.5 ± 5.0) mol % $NH_2OH$ with the remainder being $H_2O$. The gas mixtures were accurately prepared from pressure measurements using a Baratron capacitance manometer and were stored in an all glass vacuum line. To our knowledge, the first use of $NH_2OH$, as a thermal source of OH-radicals for reaction studies, was work carried out in this laboratory.[5]

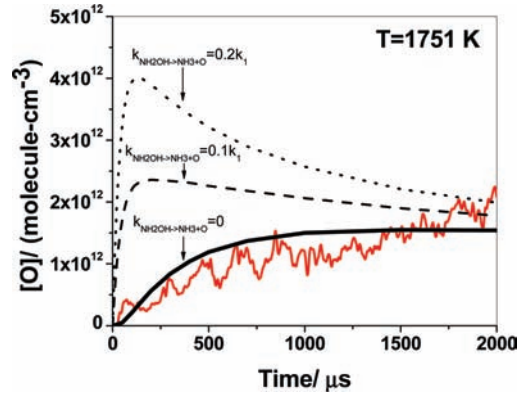


**Figure 19.** Typical O-atom profile at 1715 K with $P_1 = 15.91$ Torr, $M_s = 2.666$, $\rho_5 = 3.214 \times 10^{18}$ molecules cm$^{-3}$, [$NH_2OH$] = $2.73 \times 10^{13}$ molecules cm$^{-3}$, and [$H_2O$] = $8.83 \times 10^{14}$ molecules cm$^{-3}$. The bold line is a simulation using the mechanism of Table 10 with reaction 1 being the only dissociation process. The dotted line assumes that reactions 4 has a value that is 20% of that for 1, and the dashed line assumes a value of 10% of 1.

**O-Atom Results.** Using the previously described curve-of-growth for O-atoms,[83,84] $[O]_t$ was measured under nearly the same conditions as the OH-radical experiments described below. A typical result is shown in Figure 19 where very low levels of [O] are formed. Using the mechanism of Table 10, the result could be simulated (bold solid line) with ~3% $NH_2OH$ using only one dissociation path, namely, reaction 1. As discussed above, reactions 2a and 3 can be eliminated on theoretical grounds; however, reaction 4 is a possibility. If reaction 4 were significant then O-atom formation should be immediate and should reflect the rate of formation due to this process. In Figure 19 two simulated profiles (dotted and dashed lines) are shown where the rate constants for reaction 4 are included in the mechanism and are taken to be 20% of that for 1 (dotted line) and 10% of that for 1 (dashed line). Neither profile agrees with the measurement, strongly suggesting that reaction 4 is negligible compared to reaction 1. Hence, we conclude that, even though the energetics are favorable for (4) (see Figures 2 and 3), there is a low probability for curve crossing onto the triplet state under the present experimental conditions. We therefore need to only consider one dissociation pathway, reaction 1.

**TABLE 10: Mechanism for $NH_2OH$ Dissociation[a]**

| | | |
|---|---|---|
| $NH_2OH + Kr \rightarrow NH_2 + OH + Kr$ | $k$ to be fitted to experiment | (see Table 11) |
| $NH_2 + NH_2 \rightarrow N_2H_2 + H_2$ | $k$ from present theory | (see Table 3) |
| $NH_2 + NH_2 \rightarrow NH_3 + NH$ | $k$ from present theory | (see Table 3) |
| $H + O_2 \rightarrow OH + O$ | $k = 1.62 \times 10^{-10} \exp(-7474\ K/T)$ | 87 |
| $OH + O \rightarrow O_2 + H$ | $k = 5.42 \times 10^{-13} T^{0.375} \exp(950\ K/T)$ | 88−90 |
| $OH + OH \rightarrow O + H_2O$ | $k = 7.19 \times 10^{-21} T^{2.7} \exp(917\ K/T)$ | 88−91 |
| $OH + H_2 \rightarrow H_2O + H$ | $k = 3.56 \times 10^{-16} T^{1.52} \exp(-1736\ K/T)$ | 92 |
| $HO_2 + Kr \rightarrow H + O_2 + Kr$ | $k = 7.614 \times 10^{-10} \exp(-22520\ K/T)$ | 93 |
| $HO_2 + OH \rightarrow H_2O + O_2$ | $k = 5.00 \times 10^{-11}$ | 94 |
| $NH_2 + OH \rightarrow NH + H_2O$ | $k$ to be fitted to experiment | (see Table 11) |
| $O + H_2 \rightarrow OH + H$ | $k = 8.44 \times 10^{-20} T^{2.67} \exp(-3167\ K/T)$ | 88 |
| $OH + H \rightarrow H_2 + O$ | $k = 3.78 \times 10^{-20} T^{2.67} \exp(-2393\ K/T)$ | 88−90 |
| $H_2O + H \rightarrow OH + H_2$ | $k = 1.56 \times 10^{-15} T^{1.52} \exp(-9083\ K/T)$ | 88−90 |
| $O + H_2O \rightarrow OH + OH$ | $k = 7.48 \times 10^{-20} T^{2.7} \exp(-7323\ K/T)$ | 88−90 |
| $H_2O + Kr \rightarrow H + OH + Kr$ | $k = 2.43 \times 10^{-10} \exp(-47117\ K/T)$ | 95 |
| $N_2H_2 + Kr \rightarrow N_2 + 2H + Kr$ | $k = 8.30 \times 10^{-8} \exp(-25161\ K/T)$ | 86 |
| $NH + OH \rightarrow NO + 2H$ | $k$ from present theory | (see Table 3) |
| $NH + H \rightarrow N + H_2$ | $k = 4.98 \times 10^{-11}$ | 86 |
| $NH_2 + H \rightarrow NH + H_2$ | $k = 6.64 \times 10^{-11} \exp(-1837\ K/T)$ | 86 |
| $H + O_2 + Kr \rightarrow HO_2 + Kr$ | $k = k_{HO_2+Kr}/(7.243) \times 10^{23} \exp(-24384\ K/T)$ | 93 |
| $O + NH_3 \rightarrow OH + NH_2$ | $k = 1.56 \times 10^{-17} T^{1.94} \exp(-3251\ K/T)$ | 53 |
| $OH + NH_3 \rightarrow H_2O + NH_2$ | $k = 3.32 \times 10^{-18} T^{2.04} \exp(-285\ K/T)$ | 86 |
| $H + NH_3 \rightarrow NH_2 + H$ | $k = 1.06 \times 10^{-18} T^{2.39} \exp(-5119\ K/T)$ | 96 |
| $NH_2 + OH \rightarrow NH_3 + O$ | $k = k_{NH_3+O}/(300 T^{-0.336} \exp(-2672\ K/T))$ | 53, 97 |
| $NH_2 + O \rightarrow NO + 2H$ | $k = 1.1 \times 10^{-9} T^{-0.5}$ | 86 |
| $NH_2 + O \rightarrow OH + NH$ | $k = 1.16 \times 10^{-11}$ | 86 |
| $NH_2 + H_2O \rightarrow NH_3 + OH$ | $k = k_{NH_3+OH}/(19.8 T^{-0.3} \exp(5240\ K/T))$ | 46, 86 |
| $NH_2 + NO \rightarrow N_2 + H_2O$ | $k = 1.13 \times 10^{-8} T^{-1.203} \exp(106\ K/T)$ | 98 |
| $NH_2 + N \rightarrow N_2 + 2H$ | $k = 1.16 \times 10^{-10}$ | 86 |
| $NH_2OH + OH \rightarrow H_2O + NHOH$ | $k$ to be fitted to experiment | (see Table 11) |
| $HNOH + OH \rightarrow H + NO + H_2O$ | $k = 1.80 \times 10^{-10}$ | 99 |
| $NH + O \rightarrow OH + N$ | $k = 1.16 \times 10^{-11}$ | 53 |
| $NH + O \rightarrow H + NO$ | $k = 1.16 \times 10^{-10}$ | 46 |
| $NH + N \rightarrow N_2 + H$ | $k = 4.98 \times 10^{-11}$ | 46 |
| $NH_2 + NH \rightarrow N_2H_2 + H$ | $k$ from present theory | (see Table 3) |
| $NH + NH \rightarrow N_2 + 2H$ | $k$ from present theory | (see Table 3) |
| $NH + OH \rightarrow N + H_2O$ | $k$ from present theory | (see Table 3) |

[a] All rate constants are in $cm^3$ $molecule^{-1}$ $s^{-1}$.

**OH-Radical Results.** The temporal concentration, $[OH]_t$, from $NH_2OH$ dissociation, was determined from measured absorbance, $(ABS)_t = \ln[I_0/I_t] = [OH]_t l \sigma_{OH}$, through an earlier determination[3] of the absorption cross-section at 308 nm ($\sigma_{OH} = (4.52 - (1.18 \times 10^{-3} T)) \times 10^{-17}$ $cm^2$ $molecule^{-1}$). We used 56 or 44 optical passes (i.e., path lengths = 4.90 or 3.85 m) for these experiments. Experiments were carried out over the $T$-range 1355−1887 K and at densities between $1.09 \times 10^{18}$ and $3.29 \times 10^{18}$ molecules $cm^{-3}$.

Two typical results at 1797 and 1461 K, respectively, are shown in Figure 20 with sensitivity analyses given in Figures 21 and 22. Determination of rate constants requires chemical simulations using the reaction mechanism given in Table 10. Examination of the OH sensitive reactions shows that reactions 1, 5a, and 6a are the main reactions that determine the fits shown in Figure 20. $[OH]_t$ in the short time limit is dominated by $NH_2OH$ dissociation, reaction 1; however, to simulate $[OH]_{max}$ at any $T$, an abstraction reaction between OH and $NH_2OH$

$$OH + NH_2OH \rightarrow H_2O + NHOH \qquad (6a)$$

is required. Though theory suggests two abstraction channels, 6a and 6b, for experimental analyses we consider the dominant channel is 6a and that $NH_2O$ from 6b rapidly converts to NHOH. The main reactions contributing to subsequent OH decay are OH and $NH_2$ self-reactions and the OH + $NH_2$ cross-reaction.

$$NH_2 + OH \rightarrow NH + H_2O \qquad (5a)$$

The self-reaction of OH is well-known and cannot be varied.[88−91] The self-reaction of $NH_2$ is less well-known. The present theoretical predictions for this self-reaction [(12a)−(12d)] have been used to simulate the OH profiles (see Tables 3 and 10).

For those secondary reactions that have not been theoretically considered in this work we have relied heavily on the reaction scheme and rate constant estimates presented by Glarborg et al.[86] In general, most of the reactions have little effect on the derived results because the concentration used in this work is low, thereby de-emphasizing the effects of secondary reactions.

Over the temperature range of the experiments, 1355 K ≤ $T$ ≤ 1889 K, time resolution of the initial OH buildup is possible allowing for Table 10 mechanistic simulations giving values for $k_1$. Thirty-two values were obtained and are shown in Table 11 along with estimates for $k_{5a}$ and $k_{6a}$. The reliability of the $k_{5a}$ and $k_{6a}$ determinations is not uniform over the $T$-range. Even though the initial portions of the profiles are mostly dependent on reaction 1, adjustments in $k_{6a}$ were necessary to be compatible with the observed maximum OH yields, and the data cannot be fitted at longer times without

**TABLE 11: High-*T* Rate Data: $NH_2OH \rightarrow NH_2 + OH$ ($k_1$), $OH + NH_2OH \rightarrow HNOH + H_2O$ ($k_{6a}$) and $OH + NH_2 \rightarrow NH + H_2O$ ($k_{5a}$)**

| $P_1$/Torr | $M_s$[a] | $\rho_5/(10^{18}$ cm$^{-3})$[b] | $T_5$/K[b] | $k_1$[c] | $k_{6a}$ | $k_{5a}$ |
|---|---|---|---|---|---|---|
| | | $X_{soln}$[e] $= 4.011 \times 10^{-4}$ | | | | |
| 10.93 | 2.693 | 2.241 | 1797 | 1.38(−14) | 3.40(−11) | 3.75(−11) |
| 10.94 | 2.679 | 2.233 | 1780 | 1.12(−14) | 3.40(−11) | 3.75(−11) |
| 10.95 | 2.575 | 2.149 | 1661 | 7.45(−15) | 3.00(−11) | 3.25(−11) |
| 10.95 | 2.610 | 2.176 | 1702 | 9.19(−15) | 3.10(−11) | 3.45(−11) |
| 10.91 | 2.420 | 2.013 | 1483 | 2.33(−15) | 2.75(−11) | 2.70(−11) |
| 10.91 | 2.401 | 1.997 | 1461 | 1.10(−15) | 2.20(−11) | 2.40(−11) |
| 10.90 | 2.408 | 2.014 | 1459 | 1.24(−15) | 2.50(−11) | 2.50(−11) |
| 5.94 | 2.749 | 1.244 | 1861 | 2.09(−14) | 3.25(−11) | 3.40(−11) |
| 5.94 | 2.663 | 1.206 | 1761 | 1.24(−14) | 3.00(−11) | 3.20(−11) |
| 5.97 | 2.471 | 1.129 | 1535 | 4.43(−15) | 2.90(−11) | 2.85(−11) |
| 5.95 | 2.423 | 1.103 | 1480 | 3.04(−15) | 2.95(−11) | 2.85(−11) |
| 5.90 | 2.405 | 1.086 | 1461 | 1.15(−15) | 2.45(−11) | 2.55(−11) |
| 5.96 | 2.555 | 1.165 | 1632 | 7.13(−15) | 3.20(−11) | 3.35(−11) |
| | | $X_{soln}$[e] $= 2.950 \times 10^{-4}$ | | | | |
| 10.90 | 2.425 | 2.014 | 1490 | 2.14(−15) | 2.10(−11) | 2.80(−11) |
| 10.90 | 2.764 | 2.284 | 1889 | 1.53(−14) | 3.40(−11) | 3.65(−11) |
| 10.85 | 2.336 | 1.927 | 1392 | 6.49(−16) | 2.00(−11) | 1.80(−11) |
| 10.98 | 2.302 | 1.919 | 1355 | 5.99(−16) | 2.00(−11) | 1.50(−11) |
| 10.86 | 2.384 | 1.970 | 1444 | 1.07(−15) | 2.70(−11) | 2.30(−11) |
| 10.96 | 2.698 | 2.241 | 1812 | 1.38(−14) | 3.35(−11) | 3.55(−11) |
| | | $X_{soln}$[e] $= 3.058 \times 10^{-4}$ | | | | |
| 10.94 | 2.421 | 2.017 | 1485 | 1.88(−15) | 2.30(−11) | 2.80(−11) |
| 10.91 | 2.724 | 2.250 | 1844 | 1.42(−14) | 3.25(−11) | 3.20(−11) |
| 10.82 | 2.490 | 2.053 | 1563 | 3.90(−15) | 2.80(−11) | 3.00(−11) |
| 10.87 | 2.315 | 1.917 | 1364 | 1.04(−15) | 2.60(−11) | 2.00(−11) |
| 10.96 | 2.733 | 2.267 | 1856 | 1.54(−14) | 3.20(−11) | 3.35(−11) |
| | | $X_{soln}$[e] $= 2.268 \times 10^{-4}$ | | | | |
| 15.83 | 2.331 | 2.804 | 1386 | 1.25(−15) | 2.60(−11) | 2.40(−11) |
| 15.89 | 2.768 | 3.286 | 1887 | 1.00(−14) | 3.25(−11) | 3.50(−11) |
| 15.93 | 2.374 | 2.875 | 1433 | 1.74(−15) | 2.65(−11) | 2.45(−11) |
| 15.84 | 2.460 | 2.959 | 1526 | 3.01(−15) | 2.55(−11) | 2.95(−11) |
| 15.86 | 2.476 | 2.981 | 1544 | 2.72(−15) | 2.60(−11) | 3.00(−11) |
| 15.90 | 2.537 | 3.056 | 1612 | 5.04(−15) | 2.90(−11) | 3.10(−11) |
| 15.83 | 2.593 | 3.102 | 1677 | 6.12(−15) | 3.00(−11) | 3.25(−11) |
| 10.93 | 2.673 | 2.196 | 1781 | 1.41(−14) | 3.50(−11) | 3.75(−11) |

[a] The error in measuring the Mach number, $M_s$, is typically 0.5−1.0% at the one standard deviation level. [b] Quantities with the subscript 5 refer to the thermodynamic state of the gas in the reflected shock region. [c] Rate constants in units cm$^3$ molecule$^{-1}$ s$^{-1}$. [d] Parentheses denotes the power of 10. [e] $X_{soln} = X_{NH_2OH} + X_{H_2O}$.

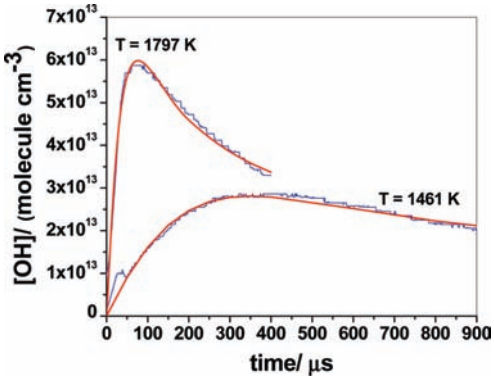


**Figure 20.** Two [OH] profiles at 1797 and 1461 K, respectively. The solid lines are temporal fits using the reaction mechanism of Table 10 with variations in $k_1$, $k_{5a}$, and $k_{6a}$. The conditions for the experiment at $T_5 = 1797$ K are $P_1 = 10.93$ Torr, $M_s = 2.693$, $\rho_5 = 2.241 \times 10^{18}$ molecules cm$^{-3}$, $[NH_2OH]_0 = 8.00 \times 10^{13}$ molecules cm$^{-3}$, and $[H_2O]_0 = 8.19 \times 10^{14}$ molecules cm$^{-3}$. The conditions for the experiment at $T_5 = 1461$ K are $P_1 = 10.91$ Torr, $M_s = 2.401$, $\rho_5 = 1.997 \times 10^{18}$ molecules cm$^{-3}$, $[NH_2OH]_0 = 8.00 \times 10^{13}$ molecules cm$^{-3}$, and $[H_2O]_0 = 7.21 \times 10^{14}$ molecules cm$^{-3}$.

adjusting the final sensitive reaction, 5a. To illustrate this point, Figure 23 depicts an example of an experiment at 1535 K in which the temporal OH profile has been fitted to a

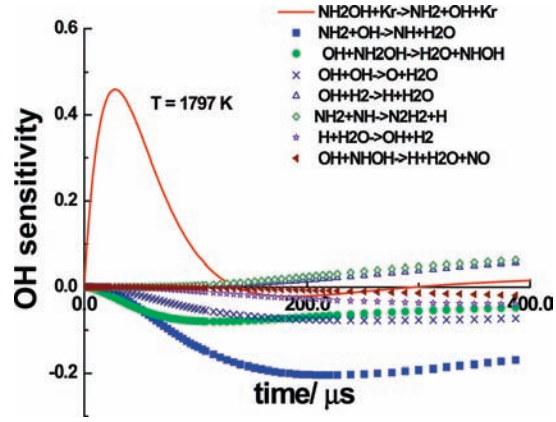


**Figure 21.** OH-radical sensitivity analysis for the 1797 K profile shown in Figure 20 using the full reaction mechanism scheme and the final fitted values for $k_1$, $k_{5a}$, and $k_{6a}$ listed in Table 10. The eight most sensitive reactions are shown in the inset.

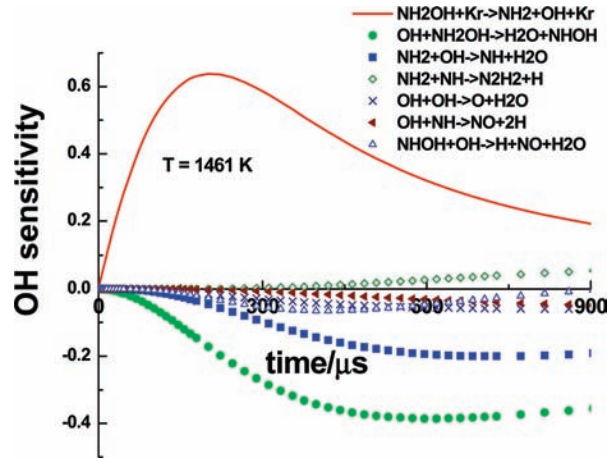


**Figure 22.** OH-radical sensitivity analysis for the 1461 K profile shown in Figure 20 using the full reaction mechanism scheme and the final fitted values for $k_1$, $k_{5a}$, and $k_{6a}$ listed in Table 10. The seven most sensitive reactions are shown in the inset.

unique set of rate constants for reactions 1, 5a, and 6a. The early time profile ($t_1 < 400$ $\mu$s) is dominated by OH formation from reaction 1. The peak [OH] and subsequent early decay ($400 < t_2 < 900$ $\mu$s) is significantly sensitive to reactions 6a, with the later decay ($t_3 > 900$ $\mu$s) being substantially dominated by reaction 5a, as seen from a brute-force sensitivity analysis depicted in the three panels of the figure. The effects of changing the rate constants by either ±20% (reaction 1) or ±30% (reaction 5a) and ±50% (reactions 6a) from the fitted rate constants degrades the quality of the fits over the three time intervals. A unique set of these three rate constants for 32 of the experiments listed in Table 11 gives profile predictions that fit the data easily to within ±10% over the entire time ranges. The values determined for each experiment are listed in the table. Hence, the mechanism of Table 10 with the values for reactions 1, 5a, and 6a gives an excellent representation of the data.

The results for $k_1$ are plotted in Arrhenius form in Figures 4 and 24. The linear-least-squares line using the experimental data shown in Figure 24 is calculated from the expression

$$\log[k_1/(\text{cm}^3\ \text{molecule}^{-1}\ \text{s}^{-1})] = (-10.12 \pm 0.20) + (-6793 \pm 317\ \text{K}/T) \quad (13)$$

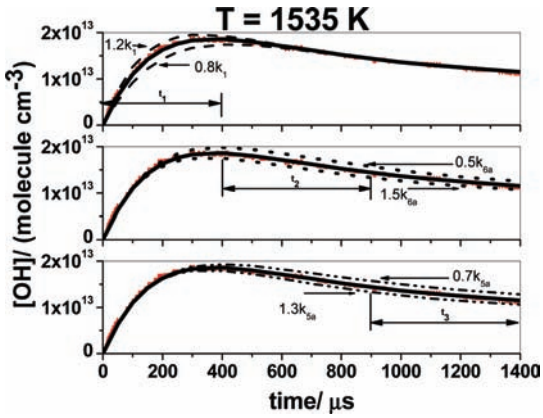


**Figure 23.** [OH] profile at 1535 K. The experimental conditions are $P_1 = 5.97$ Torr, $M_s = 2.471$, $\rho_5 = 1.129 \times 10^{18}$ molecules cm$^{-3}$, $[NH_2OH]_0 = 2.944 \times 10^{13}$ molecules cm$^{-3}$, and $[H_2O]_0 = 4.235 \times 10^{14}$ molecules cm$^{-3}$. The bold solid lines in all three panels are simulations using the full reaction mechanism scheme and the final fitted values for $k_1$, $k_{5a}$, and $k_{6a}$ listed in Table 10. Dashed lines in the upper panel: simulation using the same reaction mechanism scheme as the solid line and changing only $k_1$ by ±20%. Dotted lines in middle panel: simulation using the same reaction mechanism scheme as the solid line and changing only $k_{6a}$ by ±50%. Dash−dot−dot lines in the lower panel: simulation using the same reaction mechanism scheme as the solid line and changing only $k_{5a}$ by ±30%.

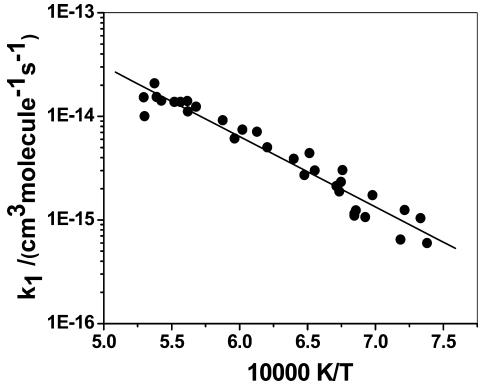


**Figure 24.** Arrhenius plot of the data for $k_1$ over the $T$-range 1355−1889 K: (●) data from present work; (solid line) least squares fit to data, eq 13.

for 1355 K ≤ $T$ ≤ 1889 K. The errors are at the one standard deviation level. The data are presented as second-order because there is no measurable pressure dependence over the limited $T$-range. Hence, eq 13 is near to the low-pressure limit. As discussed in the theoretical section, the data are in good agreement with the theory.

The data from Table 11 for reaction 6a are shown in Figures 9 and 25 as an Arrhenius plot. Though a slight $T$-dependence may be indicated, the data show substantial scatter over the limited $T$-range (1355−1889 K). Nonetheless, we derive the least-squares line using the experimental data in Figure 25 as

$$\log[k_{6a}/(\text{cm}^3\ \text{molecule}^{-1}\ \text{s}^{-1})] = (-10.00 \pm 0.06) + (-879 \pm 101\ \text{K}/T) \quad (14)$$

The data for reaction 5a from Table 11 are plotted in Arrhenius form in Figures 6, 7, and 26, again showing slight $T$-dependence. The linear-least-squares line shown in Figure 26 is calculated from the expression

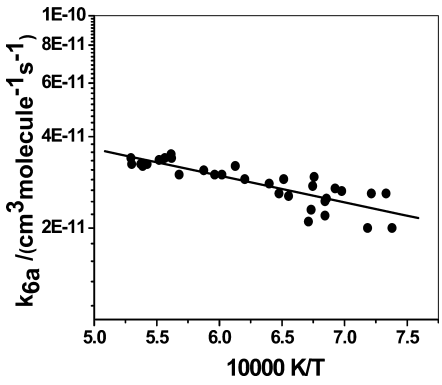


**Figure 25.** Arrhenius plot of the data for $k_{6a}$ over the $T$-range, 1355−1889 K: (●) data from present work; (solid line) least squares fit to data, eq 14.

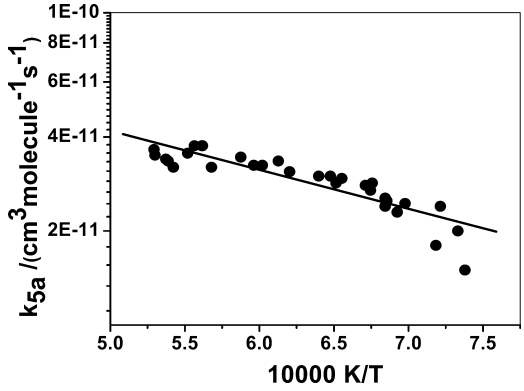


**Figure 26.** Arrhenius plot of the data for $k_{5a}$ over the $T$-range, 1355−1889 K: (●) data from present work; (solid line) least squares fit to data, eq 15.

$$\log[k_{5a}/(\text{cm}^3\ \text{molecule}^{-1}\ \text{s}^{-1})] = (-9.75 \pm 0.08) + (-1248 \pm 123\ \text{K}/T) \quad (15)$$

over the $P$- and $T$-ranges (1355−1889 K) of the experiments. The theoretical predictions for (5a) and (6a) are in good agreement with the present experimental data (see Figures 6, 7, and 9).

## Concluding Remarks

The present combined theory and experiment study demonstrates the utility of $NH_2OH$ decomposition as a high temperature source for OH. This study demonstrates that the primary products of this dissociation are $NH_2$ + OH, with little if any branching to $NH_3$ + O. The latter products have the lowest barrier to their formation, but their production requires an intersystem crossing that appears to be more rate limiting than the simple bond fission to $NH_2$ + OH.

The experimental observations of the OH time profiles provide a direct measure of the $NH_2OH$ decomposition rate over the 1355−1889 K temperature range and for pressures of a few hundred Torr. With secondary modeling these profiles have also been used to derive more approximate rate estimates for the $NH_2$ + OH and $NH_2OH$ + OH abstraction reactions.

Theoretical predictions for these reactions, as well as a number of other reactions of secondary importance to the $NH_2OH$ decomposition process, have been derived from ab initio transition state theory coupled with master equation simulations as necessary. In general, reasonably satisfactory agreement with experiment has been obtained with modest adjustments (i.e.,

within the uncertainties of the theoretical analysis) of the predicted barrier heights.

The rate estimates obtained in this work should be of considerable utility to future efforts at modeling the chemistry of $NO_x$ and the combustion of energetic materials.

**Acknowledgment.** This work was supported by the U.S. Department of Energy, Office of Basic Energy Sciences, Division of Chemical Sciences, Geosciences and Biosciences under Contract No. DE-AC02-06CH11357.

## References and Notes

(1) Glassman, I. *Combustion*, 2nd ed.; Academic Press: Orlando, 1987; p 51.
(2) Bott, J. F.; Cohen, N. *Int. J. Chem. Kinet.* **1989**, *21*, 485.
(3) (a) Srinivasan, N. K.; Su, M.-C.; Sutherland, J. W.; Michael, J. V. *J. Phys. Chem. A* **2005**, *109*, 1857. (b) Sivaramakrishnan, R.; Michael, J. V. *J. Phys. Chem. A* **2009**, *113*, 5047, and references therein.
(4) Su, M.-C.; Kumaran, S. S.; Lim, K. P.; Michael, J. V.; Wagner, A. F.; Harding, L. B.; Fang, D.-C. *J. Phys. Chem. A* **2002**, *106*, 8261.
(5) Srinivasan, N. K.; Su, M.-C.; Michael, J. V. *Phys. Chem. Chem. Phys.* **2007**, *9*, 4155.
(6) Lyon, R. K. U. S. *Pat.* **1975**, 3,900,544.
(7) Lyon, R. K. *Environ. Sci. Technol.* **1987**, *21*, 231.
(8) Miller, J. A.; Glarborg, P. *Gas Phase Chemical Reaction Systems, Experiments and Models 100 Years After Max Bodenstein*; Springer Series in Chemical Physics 61; Springer-Verlag: Berlin, Heidelberg, 1996; pp 318−333.
(9) Mackie, J. C.; Bacskay, G. B. *J. Phys. Chem. A* **2005**, *109*, 11967.
(10) Raghavachari, K.; Trucks, G. W.; Pople, J. A.; Head-Gordon, M. *Chem. Phys. Lett.* **1989**, *157*, 479.
(11) Werner, H.-J.; Knowles, P. J. *J. Chem. Phys.* **1988**, *89*, 5803.
(12) Knowles, P. J.; Werner, H.-J. *Chem. Phys. Lett.* **1988**, *145*, 514.
(13) Langhoff, S. R.; Davidson, E. R. *Int. J. Quantum Chem.* **1974**, *8*, 61.
(14) Silver, D. W.; Davidson, E. R. *Chem. Phys. Lett.* **1978**, *52*, 403.
(15) Dunning, T. H., Jr. *J. Chem. Phys.* **1989**, *90*, 1007.
(16) Kendall, R. A.; Dunning, T. H., Jr.; Harrison, R. J. *J. Chem. Phys.* **1992**, *96*, 6796.
(17) Martin, J. M. L.; Uzan, O. *Chem. Phys. Lett.* **1998**, *282*, 16.
(18) Werner, H.-J.; Knowles, P. J.; Almlof, J.; Amos, R. D.; Berning, A.; Cooper, D. L.; Deegan, M. J. O.; Dobbyn, A. J.; Eckert, F.; Elbert, S. T.; Hampel, C.; Lindh, R.; Lloyd, A. W.; Meyer, W.; Nicklass, A.; Peterson, K.; Pitzer, R.; Stone, A. J.; Taylor, P. R.; Mura, M. E.; Pulay, P.; Schutz, M.; Stoll, H.; Thorsteinsson, T. MOLPRO, 2006. 1. ed., 2006.
(19) Werner, H.-J.; Knowles, P. J. *J. Chem. Phys.* **1985**, *82*, 5053.
(20) Knowles, P. J.; Werner, H.-J. *Chem. Phys. Lett.* **1985**, *115*, 259.
(21) Haampel, C.; Peterson, K.; Werner, H.-J. *Chem. Phys. Lett.* **1992**, *190*, 1.
(22) Degan, M. J. O.; Knowles, P. J. *Chem. Phys. Lett.* **1994**, *227*, 321.
(23) Koga, N.; Morokuma, K. *Chem. Phys. Lett.* **1985**, *119*, 371.
(24) Lee, T. J.; Taylor, P. R. *Int. J. Quantum Chem.* **1989**, *23*, 199.
(25) Andersson, K.; Malmqvist, P.-A.; Roos, B. O. *J. Chem. Phys.* **1992**, *96*, 1218.
(26) Werner, H.-J. *Mol. Phys.* **1996**, *89*, 645. Celani, P.; Werner, H.-J. *J. Chem. Phys.* **2000**, *112*, 5546.
(27) Pople, J. A.; Head-Gordon, M.; Raghavachari, K. *J. Chem. Phys.* **1987**, *87*, 5968.
(28) Klippenstein, S. J. *J. Chem. Phys.* **1992**, *96*, 367.
(29) Georgievskii, Y.; Klippenstein, S. J. *J. Chem. Phys.* **2003**, *118*, 5442.
(30) Georgievskii, Y.; Klippenstein, S. J. *J. Phys. Chem. A* **2003**, *107*, 9776.
(31) Harding, L. B.; Georgievskii, Y.; Klippenstein, S. J. *J. Phys. Chem. A* **2005**, *109*, 4646.
(32) Klippenstein, S. J.; Georgievskii, Y.; Harding, L. B. *Phys. Chem. Chem. Phys.* **2006**, *8*, 1133.
(33) Miller, J. A.; Klippenstein, S. J.; Raffy, C. *J. Phys. Chem. A* **2002**, *106*, 4904.
(34) Miller, J. A.; Klippenstein, S. J. *J. Phys. Chem. A* **2006**, *110*, 10528.
(35) Troe, J. *J. Phys. Chem.* **1979**, *83*, 114.
(36) Troe, J. *Ber. Bunsen-Ges. Phys. Chem.* **1983**, *87*, 161.
(37) Miller, J. A.; Klippenstein, S. J. *J. Phys. Chem. A* **2003**, *107*, 2680.
(38) Senosiain, J. P.; Klippenstein, S. J.; Miller, J. A. *J. Phys. Chem.* **2005**, *109*, 6045.
(39) Greenwald, E. E.; North, S. W.; Georgievskii, Y.; Klippenstein, S. J. *J. Phys. Chem. A* **2005**, *109*, 6031.
(40) Fagerstrom, K.; Jodkowski, J. T.; Lund, A.; Ratajczak, E. *Chem. Phys. Lett.* **1995**, *236*, 103.
(41) Quack, M.; Troe, J. *Ber. Bunsen-Ges. Phys. Chem.* **1977**, *81*, 329.
(42) Cheskis, S. G.; Sarkisov, O. M. *Chem. Phys. Lett.* **1979**, *62*, 72.
(43) Kimball-Linne, M. A.; Hanson, R. K. *Combust. Flame* **1986**, *64*, 337.
(44) Salimian, S.; Hanson, R. K.; Kruger, C. H. *Int. J. Chem. Kinet.* **1984**, *16*, 725.
(45) Miller, J. A.; Bowman, C. T. *Prog. Energy Combust. Sci.* **1989**, *15*, 287.
(46) Cohen, N.; Westberg, K. R. *J. Phys. Chem. Ref. Data* **1991**, *20*, 1211.
(47) Dean, A. M.; Bozzelli, J. W. In *Combustion Chemistry II*; Gardiner, W. C., Ed.; Springer: New York, 2001.
(48) Xu, Z.-F.; Fang, D.-C.; Fu, X.-Y. *Theor. Chem. Acc.* **2000**, *104*, 7.
(49) Rohrig, M.; Wagner, H. G. *Proc. Combust. Inst.* **1994**, *25*, 975.
(50) Ruscic, B.; Pinzon, R. E.; Morton, M. L.; von Laszewski, G.; Bittner, S.; Nijsure, S. G.; Amin, K. A.; Minkoff, M.; Wagner, A. F. *J. Phys. Chem. A* **2004**, *108*, 9979. Ruscic, B.; Pinzon, R. E.; von Laszewski, G.; Kodeboyina, D.; Burcat, A.; Leahy, D.; Montoya, D.; Wagner, A. F. *J. Phys. Conf. Ser.* **2005**, *16*, 561.
(51) Ruscic, B. Unpublished results obtained from Active Thermochemical Tables (ref 50) ver. 1.37 and the Core (Argonne) Thermochemical Network ver. 1.074 (2009).
(52) Baulch, D. L.; Bowman, C. T.; Cobos, C. J.; Cox, R. A.; Just, T.; Kerr, J. A.; Pilling, M. J.; Stocker, D.; Troe, J.; Tsang, W.; Walker, R. W.; Warnatz, J. *J. Phys. Chem. Ref. Data* **2005**, *34*, 757.
(53) Sutherland, J. M.; Patterson, P. M.; Klemm, R. B. *J. Phys. Chem.* **1990**, *94*, 2471.
(54) Perry, R. A. *Chem. Phys. Lett.* **1984**, *106*, 223.
(55) Sumathi, R.; Sengupta, D.; Nguyen, M. T. *J. Phys. Chem. A* **1998**, *102*, 3175.
(56) Hack, W.; Kurzke, H. *Ber. Bunsen-Ges. Phys. Chem.* **1985**, *89*, 86.
(57) Townsend, D.; Lahankar, S. A.; Lee, S. K.; Chambreau, S. D.; Suits, A. G.; Zhang, X.; Rheinecker, J.; Harding, L. B.; Bowman, J. M. *Science* **2004**, *306*, 1158.
(58) Mertens, J. D.; Chang, A. Y.; Hanson, R. K.; Bowman, C. T. *Int. J. Chem. Kinet.* **1989**, *21*, 1049.
(59) Kajimoto, O.; Kondo, O.; Okada, K.; Fujikane, J.; Fueno, T. *Bull. Chem. Soc. Jpn.* **1985**, *58*, 3469.
(60) Hori, K.; Oya, M.; Tanaka, H.; Asaba, T. *Symp. (Int.) Shock Waves Shock Tubes, 15th* **1985**, 261.
(61) Nicholas, J. E.; Spiers, A. I.; Matin, N. A. *Plasma Chem. Plasma Proc.* **1986**, *6*, 139.
(62) Xu, Z.-F.; Fang, D.-C.; Fu, X.-Y. *Chem. Phys. Lett.* **1997**, *275*, 386.
(63) Bahng, M.-K.; Macdonald, R. G. *J. Phys. Chem. A* **2009**, *113*, 2415.
(64) Davidson, D. F.; Kohse-Hoinghaus, K.; Chang, A. Y.; Hanson, R. K. *Int. J. Chem. Kinet.* **1990**, *22*, 513.
(65) Dransfeld, P.; Kurzke, H.; Temps, F.; Wagner, H. G. *Proc. Combust. Inst.* **1984**, *20*, 655.
(66) Pagsberg, P. B.; Eriksen, J.; Christensen, H. C. *J. Phys. Chem.* **1979**, *83*, 582.
(67) Salimian, S.; Hanson, R. K.; Kruger, C. H. *Combust. Flame* **1984**, *56*, 83.
(68) Hwang, D.-Y.; Mebel, A. M. *J. Phys. Chem. A,* **2003**, *107*, 2865.
(69) Xu, Z.-F.; Fang, D.-C.; Fu, X.-Y. *Int. J. Quantum Chem.* **1998**, *70*, 321.
(70) Rohrig, M.; Romming, H.-J.; Wagner, H. G. *Ber. Bunsen-Ges. Phys. Chem.* **1994**, *98*, 1332.
(71) Gordon, S.; Mulac, W.; Nangia, P. *J. Phys. Chem.* **1971**, *75*, 2087.
(72) Back, R. A.; Yokota, T. *Int. J. Chem. Kinet.* **1973**, *5*, 1039.
(73) Khe, P. V.; Soulignac, J. C.; Lesclaux, R. *J. Phys. Chem.* **1977**, *81*, 210.
(74) Lozovskii, V. A.; Nadtochenko, V. A.; Sarkisov, O. M.; Cheskis, S. G. *Kinet. Catal.* **1979**, *20*, 918.
(75) Sarkisov, O. M.; Cheskis, S. G.; Nadtochenko, V. A.; Sviridenkov, E. A.; Vedeneev, V. I. *Arch. Combust.* **1984**, *4*, 111.
(76) Bahng, M.-K.; Macdonald, R. G. *J. Phys. Chem. A* **2008**, *112*, 13432.
(77) Stothard, N.; Humpfer, R.; Grotheer, H.-H. *Chem. Phys. Lett.* **1995**, *240*, 474.
(78) Michael, J. V. *Prog. Energy Combust. Sci.* **1992**, *18*, 327.
(79) Michael, J. V. In *Advances in Chemical Kinetics and Dynamics*; Barker, J. R., Ed.; JAI: Greenwich, U.K., 1992; Vol. I, pp 47−112, for original references.
(80) Michael, J. V.; Sutherland, J. W. *Int. J. Chem. Kinet.* **1986**, *18*, 409.
(81) Michael, J. V. *J. Chem. Phys.* **1989**, *90*, 189.

(82) Michael, J. V.; Fisher, J. R. In *Seventeenth International Symposium on ShockWaves and Shock Tubes*; Kim, Y. W., Ed.; AIP Conference Proceedings 208; American Institute of Physics: New York, 1990; pp 210−215.

(83) Michael, J. V.; Lim, K. P. *J. Chem. Phys.* **1992**, *97*, 3228.

(84) Michael, J. V.; Kumaran, S. S.; Su, M.-C. *J. Phys. Chem. A* **1999**, *103*, 5942.

(85) Su, M.-C.; Kumaran, S. S.; Lim, K. P.; Michael, J. V. *Rev. Sci. Instrum.* **1995**, *66*, 4649.

(86) Glarborg, P.; Dam-Johansen, K.; Miller, J. A. *Int. J. Chem. Kinet.* **1995**, *27*, 1207.

(87) Du, H.; Hessler, J. P. *J. Chem. Phys.* **1992**, *96*, 1077.

(88) Michael, J. V. *Prog. Energy Combust. Sci.* **1992**, *18*, 327.

(89) Ruscic, B.; Wagner, A. F.; Harding, L. B.; Asher, R. L.; Feller, D.; Dixon, D. A.; Peterson, K. A.; Song, Y.; Qian, X.; Ng, C. Y.; Liu, J.; Chen, W.; Schwenke, D. W. *J. Phys. Chem. A* **2002**, *106*, 2727.

(90) Herbon, J. T.; Hanson, R. K.; Golden, D. M.; Bowman, C. T. *Proc. Combust. Inst.* **2002**, *29*, 1201.

(91) Wooldridge, M. S.; Hanson, R. K.; Bowman, C. T. *Int. J. Chem. Kinet.* **1994**, *26*, 389.

(92) Oldenborg, R. C.; Loge, G. W.; Harridine, D. M.; Winn, K. R. *J. Phys. Chem.* **1992**, *96*, 8426.

(93) Michael, J. V.; Su, M.-C.; Sutherland, J. W.; Carroll, J. J.; Wagner, A. F. *J. Phys.Chem. A* **2002**, *106*, 5297.

(94) Srinivasan, N. K.; Su, M.-C.; Sutherland, J. W.; Michael, J. V.; Ruscic, B. *J. Phys. Chem. A* **2006**, *110*, 6602.

(95) Srinivasan, N. K.; Michael, J. V. *Int. J. Chem. Kinet.* **2005**, *38*, 211.

(96) Michael, J. V.; Sutherland, J. W.; Klemm, R. B. *J. Phys. Chem.* **1986**, *90*, 497.

(97) Ruscic, B. Unpublished results obtained from Active Thermochemical Tables (ref 50) ver. 1.25 and the Core (Argonne) Thermochemical Network ver. 1.049 (2005).

(98) Song, S.; Hanson, R. K.; Bowman, C. T.; Golden, D. M. *Int. J. Chem. Kinet.* **2001**, *33*, 715.

(99) Sun, F.; DeSain, J. D.; Scott, G.; Hung, P. Y.; Thompson, R. I.; Glass, G. P.; Curl, R. F. *J. Phys.Chem. A* **2001**, *105*, 6121.

JP905454K